Faraday Discussions

Accepted Manuscript

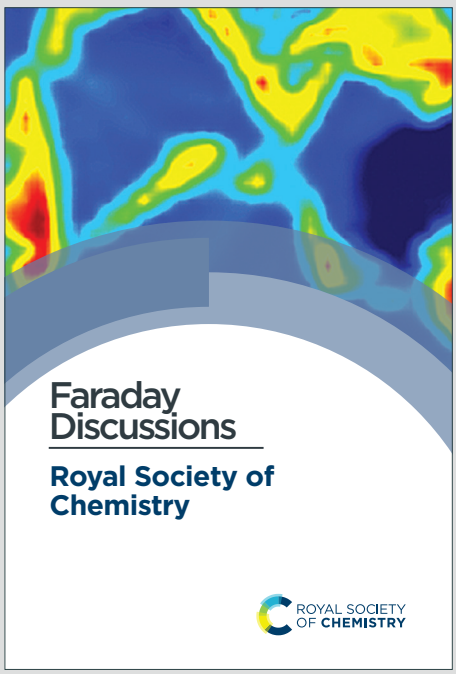

This article can be cited before page numbers have been issued, to do this please use: G. Grell, J. Galiana, S. M. Cavaletto, J. Gonzalez-Vazquez, A. Palacios and F. Martín, *Faraday Discuss.*, 2026, DOI: 10.1039/D6FD00086J.

View Article Online
DOI: 10.1039/D6FD00086J

Journal Name

ARTICLE TYPE

Cite this: DOI: 00.0000/xxxxxxxxxx

Advances in the Projected Forces and Momenta Decoherence Method for Attosecond Nonadiabatic Molecular Dynamics

Gilbert Grell[a†], Joachim Galiana[b], Stefano M. Cavaletto[b], Jesús González-Vázquez[b], Alicia Palacios[b,c], and Fernando Martín[a,b,ᵡ]

Received Date
Accepted Date

DOI: 00.0000/xxxxxxxxxx

The Projected Forces and Momenta (PFM) decoherence correction has been recently introduced [*J. Chem. Theory Comput. 2025, 21, 10645*] and successfully applied for trajectory surface-hopping (TSH) simulations describing the coupled electron-nuclear dynamics originating from coherent superpositions of molecular electronic states generated by broadband laser excitation. In this work, we extend the capabilities of TSH-PFM for the simulation of a broader range of nonadiabatic dynamics. First, we showcase the inclusion of the explicit interaction with a broadband pulse and apply it to the LiH molecule, obtaining very good agreement with full quantum-mechanical reference calculations. We then demonstrate how a recently proposed post-processing approach to incorporate a posteriori initial electronic coherences onto pulse-independent TSH trajectories [*J. Chem. Theory Comput. 2026, 22, 1224*] allows for the evaluation of the dynamics arising from initial electronic coherences across a large manifold of few-fs UV pulses, without recalculating the nuclear dynamics for every set of parameters. This is exemplified for the glycine molecule, systematically varying the central frequency and bandwidth of the broadband excitation pulse. Finally, we scrutinize TSH-PFM for the ring-opening reaction in 1,2-dithiane. On the one hand, we show that TSH-PFM predicts the same nonadiabatic dynamics as established TSH approaches throughout the whole propagation of 700 fs. On the other hand, we find that an initial superposition of the two lowest excited states, albeit decohering before the ring opens, accelerates the structural dynamics by several tens of fs compared to that starting exclusively from the lowest excited state due to the population of the second excited state.

1 Introduction

For almost two decades, attosecond XUV pulses and, more recently, x-ray pulses with bandwidths as large as 10 eV or more [1–4] have been used to ionize molecules, leaving the residual molecular cation in a coherent superposition of electronic states. [5–12] The recent production of few-fs [13–16] and attosecond [17] UV pulses with bandwidths of several eV has opened the way to generate electronic coherences in neutral molecules, heralding a new era in attochemistry. [18–21] In both scenarios, the coupled electron-nuclear dynamics that follows the interaction with the incoming pulse is expected to be different from that starting from a single electronic state, the only possibility for neutral molecules until very recently. Since a full quantum mechanical description of such coherent dynamics rapidly becomes unfeasible for polyatomic molecules involving several simultaneously populated electronic potentials [22,23], mixed quantum-classical methods, in which nuclear motion is described classically while electrons are treated quantum mechanically, are the most practical option for medium-size and large molecules. [24]

The Trajectory Surface Hopping (TSH) method propagates the system at any given time along the gradient of a single, i.e., the active, electronic potential. Nonadiabatic couplings (NACs) permit the trajectory to stochastically hop to a different electronic potential, allowing an ensemble of trajectories to branch and follow different gradients. [25,26] This capability is instrumental to model nonadiabatic molecular dynamics, such as passages through conical intersections [27,28], and a major reason why TSH became one

[a]*Instituto Madrileño de Estudios Avanzados en Nanociencia (IMDEA-Nanociencia), Cantoblanco, 28049 Madrid, Spain.*
[b]*Departamento de Química, Módulo 13, Universidad Autónoma de Madrid, 28049 Madrid, Spain*
[c]*Condensed Matter Physics Center (IFIMAC), Universidad Autónoma de Madrid, 28049 Madrid, Spain.*
[†]*E-mail: gilbert.grell@imdea.org*
[ᵡ]*E-mail: fernando.martin@uam.es*

View Article Online
DOI: 10.1039/D6FD00086J

of the most popular methods to simulate such dynamics in larger molecules, in particular in the framework of femtochemistry.[29–36] In that, the development of methods to incorporate decoherence effects due to the decreasing overlap between nuclear wave packets moving on different electronic potentials critically improved the reliability of TSH calculations[37–55] by mitigating the overly coherent character due to the classical treatment of the nuclei. These methods have been designed mainly for situations where the trajectory ensemble comprises a narrow distribution of total energies, as in femtochemistry, owing to the relatively narrow bandwidth of the employed lasers, which excite in most cases only a single electronic state. Modeling the dynamics of initial electronic coherences with TSH has, in turn, only recently entered the focus, with several theoretical works highlighting the strong sensitivity of electronic properties to the description of decoherence.[56–59]

In this context, the Projected Forces and Momenta (PFM) decoherence correction has been recently introduced.[59] The PFM decoherence is estimated from the active-potential and inactive-potential forces and momenta projected onto the direction of the trajectory velocity vector, which requires only the minimum ingredients for TSH, i.e., the active-potential gradient and the potential energies at every time step.[59] TSH-PFM calculations thus bear no additional cost with respect to established decoherence approaches[45,46,50] and avoid the expensive evaluation of inactive-potential gradients and nonadiabatic coupling matrix elements required in other promising methods.[47,48,53,55]

So far, TSH-PFM has been tested with encouraging results against quantum-mechanical calculations in diatomic and medium-size polyatomic molecules[59] when starting from a predefined coherent superposition of states, reflecting an instantaneous excitation by a broadband pulse. However, the coupled electron-nuclear dynamics may be further affected by the exciting pulse as the electronic coherence builds up.[60,61] It thus remains to be seen if TSH-PFM can provide a similarly accurate description of the coherent dynamics in the presence of the pulse, in particular because the decoherence correction has been demonstrated to be very important for such dynamics.[62] Several methods to explicitly include external fields into TSH have already been proposed[32], for instance, field-induced surface hopping (FISH)[63,64] and surface hopping including arbitrary couplings (SHARC).[65,66] In this work, we adopt the latter, as it incorporates the effect of the laser onto the electronic potentials. As a first step towards the implementation of the full-dimensional PFM decoherence for the SHARC approach with external fields, we restrict ourselves to the less approximate one-dimensional case[59], and test the implementation on a two-state model of the LiH molecule[67–69] irradiated by a sub-cycle UV pulse. We find good agreement with previously reported quantum-mechanical results for the populations, as well as for the coherent oscillations in the electronic dipole.[67]

An important limitation of any nonadiabatic molecular dynamics methodology is that the evaluation of actual experimental observables, such as time-resolved photoelectron, photo-ion or photo-absorption spectra, is computationally demanding for polyatomic molecules. In the case of TSH, one has to evaluate the respective matrix elements at every time-step for each trajectory, likely amounting to many tens of thousands in neutral molecules, and even hundreds of thousands in molecular cations due to the larger number of electronic states involved in the initial coherent superposition. Although this is not impossible, the huge computational cost prevents one from investigating potential control schemes by varying the pulse parameters, since, for every choice of these parameters, a new ensemble of TSH trajectories and corresponding matrix elements should be evaluated. In this work, we use a recently proposed post-processing approach[70] which allows one to include a posteriori the effect of different initial electronic coherences onto precomputed pulse-independent TSH-PFM trajectories, i.e., trajectories obtained independently of the specific details of the pump pulse and of the coherences it generates. This is achieved by re-propagating just the electronic dynamics along the existing trajectories without any further electronic structure calculations, which is reminiscent of the concept of time-displaced basis functions used in different methods.[71–73] We employ this methodology to systematically study the evolution of initial coherences in glycine by varying the central frequency and bandwidth of the few-fs UV exciting pulse. We thereby show that by changing the parameters of the pulse, not only the initial coherences can be controlled, but also, to some extent, the frequency of their oscillations, providing preliminary scenarios to maximize and minimize the effect of such coherences.

So far, TSH-PFM applications mainly focused on the dynamics during the first few tens of femtoseconds after the excitation, where structural changes are not very pronounced. Here we also employ TSH-PFM to simulate the ring-opening and ring-closure dynamics occurring with a period of about 310 fs in excited 1,2-dithiane, a well-known model system for strongly nonadiabatic dynamics, as the potentials of the ground, S_0, and excited states, S_1, S_2, become degenerate and strongly coupled during the process.[74–77] We show that TSH-PFM predicts exactly the same structural dynamics as TSH with the well-established energy-based decoherence correction (TSH-EDC)[45] and without decoherence (TSH-ND)[25,26] for 700 fs of the dynamics, demonstrating its reliability at long time scales. In addition, we find that an initial S_1-S_2 coherence survives for about 10 fs, i.e., before the onset of the ring-opening. Interestingly, we observe that the additional population in the S_2 state of this coherent superposition accelerates the opening and closing of the ring by about 30 fs with respect to the dynamics in the purely S_1-excited species.

2 Theoretical methods

The theoretical methods have been discussed in detail elsewhere.[59,65,70] Here we summarize the basic ingredients relevant for the description of the dynamics of initial coherences and the inclusion of an explicit laser pulse into TSH-PFM simulations.

2.1 The TSH-PFM approach

Following the original definition of TSH[25,26], the quantum state at time t and nuclear configuration, $\boldsymbol{R}(t)$, is given by

$$|\Psi(t)\rangle = \sum_j c_j(t)|\psi_j;\boldsymbol{R}(t)\rangle \quad (1)$$

View Article Online
DOI: 10.1039/D6FD00086J

Here, $|\psi_j;\boldsymbol{R}(t)\rangle$ and $c_j(t)$, respectively, denote the jth adiabatic electronic state, parameterically depending on $\boldsymbol{R}(t)$, and the associated complex electronic coefficient, while the sum encompasses all electronic potentials, j, that are included in the propagation. For an initial coherence, the zero-time coefficients, $c_j(0)$, correspond to the respective quantum amplitudes induced by the excitation. Starting from the initial positions, $\boldsymbol{R}(0)$, momenta, $\boldsymbol{P}(0)$, electronic coefficients, $\boldsymbol{c}(0)$, and active electronic potential, $a(0)$, every trajectory, $\boldsymbol{R}(t)$, is obtained by classically propagating along the forces in the active electronic potential. The electronic coefficients are propagated by integrating the time-dependent Schrödinger equation (TDSE),

$$\mathrm{i}\dot{c}_j(t) = \sum_k \left[H_{jk}(\boldsymbol{R}(t)) - \mathrm{i}T_{jk}(\boldsymbol{R}(t))\right] c_k(t) \tag{2}$$

where $H_{jk}(\boldsymbol{R}(t))$ denotes the Hamiltonian matrix element between the electronic states j,k and $T_{jk}(\boldsymbol{R}(t)) = \langle\psi_j;\boldsymbol{R}(t)|\partial_t|\psi_k;\boldsymbol{R}(t)\rangle$ is the time-derivative coupling due to the variation of the electronic states along the trajectory $\boldsymbol{R}(t)$. In a basis of adiabatic states, the Hamiltonian is diagonal, $H_{jk}(\boldsymbol{R}(t)) = \mathscr{E}_j(\boldsymbol{R}(t))\delta_{jk}$, where $\mathscr{E}_j(\boldsymbol{R}(t))$ are the corresponding potential energy surfaces and $T_{jk}(\boldsymbol{R}(t))$ is related to the NAC between the adiabatic states j,k.

The decoherence correction is incorporated at the end of every TDSE integration time step, δt, after the surface hopping procedure has been carried out, by damping the adiabatic inactive-potential coefficients, with the decoherence rate $k_{ia}(t)$, i.e., $c_i(t) = c_i(t)\mathrm{e}^{-k_{ia}(t-\delta t)\delta t}$ and redistributing the population to the active potential.[42,43,45,59] Here and in the following, indices a and i, respectively, denote active and inactive potentials, while j,k denote all electronic potentials.

Abbreviating the arguments $\boldsymbol{R}(t) \to t$, the PFM decoherence rate reads.

$$k_{ia}^{\mathrm{PFM}}(t) = \frac{\pi^2}{8\omega}|P_{ia}^{\mathrm{v}}(t)||F_{ia}^{\mathrm{v}}(t)| + |P_{ia}^{\mathrm{v}}(t)|\sqrt{\frac{\pi^2 N_D \omega}{8}} \tag{3}$$

It is determined by the differences between the mass-weighted active-potential and inactive-potential forces and momenta projected onto the direction of the mass-weighted trajectory velocity vector, $F_{ia}^{\mathrm{v}}(t) = F_i^{\mathrm{v}}(t) - F_a^{\mathrm{v}}(t)$ and $P_{ia}^{\mathrm{v}}(t) = P_i^{\mathrm{v}}(t) - P_a^{\mathrm{v}}(t)$, as well as by the geometrical average over the normal-mode frequencies, ω, and the number of vibrational degrees of freedom, N_D.[59] The auxiliary momenta, $P_j^{\mathrm{v}}(t)$, are approximately propagated according to the auxiliary forces, $F_j^{\mathrm{v}}(t)$, which are related to the time-derivatives of the adiabatic potential energies. We further include the active-potential momentum injection mechanism into the inactive-potential auxiliary momentum propagation. Energy conservation in case of potential hops is taken into account by isotropic velocity rescaling, and properly translated into the auxiliary momentum propagation. See Ref. 59 for details.

2.2 Inclusion of external fields

The interaction with a laser pulse is incorporated following the SHARC approach[65] by including the field-induced couplings into the, now explicitly time-dependent, Hamiltonian, in Eq. (2),

$$H'_{jk}(\boldsymbol{R}(t),t) = H_{jk}(\boldsymbol{R}(t)) - \boldsymbol{d}_{jk}(\boldsymbol{R}(t))\cdot\boldsymbol{E}(t) \tag{4}$$

where $\boldsymbol{d}_{jk}(\boldsymbol{R}(t))$ is the electronic dipole matrix element between the adiabatic states j,k, and $\boldsymbol{E}(t)$ is the electric field of the pulse. In practice, we diagonalize the Hamiltonian matrix, $H'_{jk}(\boldsymbol{R}(t),t)$, at every time step to obtain the field-adiabatic electronic potentials, $\mathscr{E}_j^f(\boldsymbol{R}(t),t)$, electronic states, $|\psi_j^f(t);\boldsymbol{R}(t)\rangle$, and coefficients, $c_j^f(t)$, by integrating the TDSE, Eq. (2). The field-adiabatic basis is also used to evaluate the nuclear dynamics, surface hopping and decoherence. The respective forces, $\boldsymbol{F}_j^f(\boldsymbol{R}(t),t) = -\boldsymbol{\nabla}\mathscr{E}_j^f(\boldsymbol{R}(t),t)$, couple the gradients of the field-free adiabatic potentials and are evaluated numerically for every component, α, diagonalizing the Hamiltonian at distances, $\boldsymbol{R}(t) \pm \Delta R\boldsymbol{e}_\alpha$.[65]

As a first step for the implementation of TSH-PFM for multi-dimensonal dynamics in the presence of a field, we restrict ourselves to the one-dimensional case where direct comparison with full quantum calculations is feasible. The forces and momenta thus become scalar quantities and the projection onto the trajectory velocity, central for the PFM decoherence correction, Eq. (3), is not meaningful anymore. Instead, the one-dimensional forces and momenta (FM) decoherence rate without this approximation[44,59] has to be employed. Abbreviating the arguments $\boldsymbol{R}(t),t \to t$, the FM decoherence for a diatomic in the presence of a laser field is,

$$k_{ia}^{\mathrm{FM}}(t) = \frac{\sigma^2}{2}\left(P_{ia}^f(t)F_{ia}^f(t) + |P_{ia}^f(t)|\sqrt{F_{ia}^f(t)^2 + \frac{1}{\mu^2\sigma^6}}\right) \tag{5}$$

which contains the reduced mass, μ, the vibrational ground-state wave function width, σ, and the respective field-adiabatic inactive-active momentum and force differences, $P_{ia}^f(t)$ and $F_{ia}^f(t)$.

In the presence of a laser, the energy to conduct a surface hop is assumed to be absorbed from the field and no energy-conserving correction is applied to the trajectory velocity if the hop occurs to a potential within the laser bandwidth.[65] This has to be taken into account for the propagation of the auxiliary inactive-potential momenta for the FM decoherence rate in Eq. (5) as well, requiring an adaptation of the energy-conserving propagation as described in Section 2.6 of Ref. 59, see Supplementary Information (SI) for details.

2.3 Post-processing of pump-induced coherences

To account for variations of the initial pulse in a more flexible way, we have proposed in Ref. 70 to post-process the initial electronic coherences by re-propagating the electronic TDSE along a set of pre-computed, pulse-independent trajectories. To do so, we define the so-called All eXcited-state Ensemble (AXE) considering a set of initial conditions $\{\nu\} = \{(g,a)\}$ running over a distribution of N_g initial geometries and momenta, $\{\boldsymbol{R}^{(g)}(0), \boldsymbol{P}^{(g)}(0)\}$, and the included $(N_s - 1)$ excited states. These initial conditions assume that only the active electronic potential a is populated at $t = 0$, so that pulse-induced electronic coherences are not taken into account and need not to be known at this stage. This yields the trajectories, $\boldsymbol{R}^{(\nu)}(t)$, from which all necessary matrix elements

View Article Online
DOI: 10.1039/D6FD00086J

required to evaluate the desired observables for any operator $\hat{A}$, acting on the electronic subspace, $\langle \psi_j; \boldsymbol{R}^{(\nu)}(t)|\hat{A}|\psi_k; \boldsymbol{R}^{(\nu)}(t)\rangle$, can be computed.

The pulse-induced coherences are then included as follows. First, initial electronic coefficients, $c_j^{(\nu)}(0)$, are defined, e.g., by solving the TDSE in the presence of the field in frozen nuclei approximation or from first-order perturbation theory. The evolution of these initial coherences is then obtained by re-propagating the electronic TDSE, Eq. (2), along the previously computed and now frozen trajectories, $\boldsymbol{R}^{(\nu)}(t)$. The so obtained re-propagated electronic coefficients are indicated as $C_j^{(\nu)}(t)$ in the following, whereas $c_j^{(\nu)}(t)$ denotes the coefficients obtained by jointly propagating the coupled electron-nuclear TSH dynamics starting from the same initial conditions, $c_j^{(\nu)}(0)$, as discussed in Sec. 2.1.

The underlying assumption is that the NAC is weak during the survival of the initial coherences and acts independent of them, since the surface hops happen in the exact same manner as in the precomputed trajectories. It is equivalent to assuming that the coherences themselves do not influence the nuclear dynamics or that there is no conical intersection in the Franck-Condon region.[60,70] The electronic wave packets obtained by re-propagation, $|\Phi^{(\nu)}(t)\rangle = \sum_j C_j^{(\nu)}(t)\,|\psi_j; \boldsymbol{R}^{(\nu)}(t)\rangle$, are then used to evaluate the expectation value of an operator $\hat{A}$, acting only on the electronic subspace. For an individual trajectory, $\boldsymbol{R}^{(\nu)}(t)$, one has

$$\begin{aligned} A^{(\nu)}(t) &= \langle \Phi^{(\nu)}(t)|\hat{A}|\Phi^{(\nu)}(t)\rangle \\ &= \sum_{j,k} [C_j^{(\nu)}(t)]^* C_k^{(\nu)}(t) \underbrace{\langle \psi_j; \boldsymbol{R}^{(\nu)}(t)|\hat{A}|\psi_k; \boldsymbol{R}^{(\nu)}(t)\rangle}_{A_{jk}(\boldsymbol{R}^{(\nu)}(t))} \end{aligned} \tag{6}$$

allowing one to include the evolution of the initial electronic coherences a posteriori into the simulated observables. For a fully propagated TSH trajectory ν, as discussed in Secs. 2.1 and 2.2, the expectation values $A^{(\nu)}(t)$ can be similarly obtained via Eq. Eq. (6), by replacing the re-propagated wave packet $|\Phi^{(\nu)}(t)>$ and electronic coefficients $C_j^{(\nu)}(t)$ with fully propagated ones, $|\psi^{(\nu)}(t)>$ and $c_j^{(\nu)}(t)$, respectively. A given observable is obtained as a weighted average of the individual expectation values over the respective trajectory ensemble,

$$A(t) = \sum_{\nu=1}^{N_t} W^{(\nu)} A^{(\nu)}(t) \tag{7}$$

where $W^{(\nu)}$ encodes the weight of the initial condition, $\nu = (g,a)$, that is, the probability to excite the initial geometry, g, and electronic state, a, at $t = 0$.[70]

In this manner any electronic observable can be computed without recalculating the trajectories nor the, usually expensive, electronic matrix elements required for the evaluation of, e.g., ionization probabilities. The simulation can thus be performed for as many initial pulses as desired, only for the numerical cost of solving the electronic TDSE for each pulse along frozen trajectories. The accuracy of this post-processing approach has been demonstrated in previous work on glycine by comparing with results from TSH-PFM calculations in which the initial electronic coherences were included from the very beginning of the simulations.[70]

2.4 Computational details

All TSH calculations have been carried out with a local modification of the SHARC code.[65,78] The respective TSH algorithm is detailed in Ref. 59. The positions of the atomic nuclei are propagated with the Velocity-Verlet algorithm. The 4th order Runge-Kutta method is used to integrate the TDSE, Eq. (2), for the electronic coefficients in a local diabatic basis[79,80], utilizing 51 sub-steps between two nuclear time steps, i.e., configurations $\boldsymbol{R}(t)$ and $\boldsymbol{R}(t+\Delta t)$. However, the (field-) adiabatic basis is employed to evaluate the nuclear dynamics, surface hopping, utilizing the density-flux hopping probability[64], and decoherence. For the propagation of the inactive-potential auxiliary momenta to evaluate the PFM and FM decoherence rates, Eqs. (3) and (5), an inactive-potential population threshold of $\eta = 10^{-4}$, is employed, indicating that auxiliary wave packets in inactive potentials with less population are assumed to be fully decohered. See Ref.[59] and the SI for details.

The electronic structure for all molecules was evaluated using the state-averaged (SA) complete active space self consistent field (CASSCF) method[81,82] as implemented in the OPENMOLCAS package.[83] The time-derivative couplings are estimated by using finite differences with the overlap matrix elements between the wave functions of consecutive nuclear time steps, $\langle \psi_j; \boldsymbol{R}(t+\Delta t)|\psi_k; \boldsymbol{R}(t)\rangle$.[38] In case of a surface hop in absence of an external laser field, the velocity vector of the trajectory is rescaled such as to conserve the total energy. If the kinetic energy is too small to cover the potential gap in case of a hop to a higher potential, the hop is frustrated, i.e., not carried out, without modifying the velocity vector.

The initial positions and momenta, $\{\boldsymbol{R}^{(\nu)}(0), \boldsymbol{P}^{(\nu)}(0)\}$, for the $\nu = 1,...,N_t$ trajectories are sampled from the harmonic approximation of the neutral ground-state nuclear Wigner distribution at zero temperature[84] for all molecules. The optimized geometries and harmonic frequencies are given in the SI for all molecules. If starting the propagation from an initial coherent superposition with several nonzero initial electronic coefficients, $c_j^{(\nu)}(0) \neq 0$, the initial active potential, $a(0) = j$, is chosen randomly with the probability $|c_j^{(\nu)}(0)|^2$ for each trajectory, $\boldsymbol{R}^{(\nu)}(t)$. After the propagation has finished, trajectories whose total energy has drifted by more than a threshold, $\mathscr{E}_D$, are excluded from the evaluation of the ensemble averages, as they violate energy conservation. Since trajectories started in different initial active potentials may exhibit varying stability and thus a disproportionate removal of trajectories started in a certain active potential, stochastic balancing is applied after removal of those trajectories that violate total energy conservation, see Ref.[59] for details.

2.4.1 Lithium hydride

We consider a two-state model for the LiH molecule that has been extensively studied in the context of multiple-spawning[67–69] and other TSH[69] approaches for simulating coherent dynamics induced by non-perturbative laser pulses. Replicating the respec-

View Article Online
DOI: 10.1039/D6FD00086J

tive SA(2)-CASSCF(4,6) electronic structure, with the 6-31G basis set, the S_0 and S_1 states are simultaneously optimized with an active space allowing configurations in which the four electrons of the system are distributed among the six lowest orbitals. With this approach, the equilibrium bond distance was optimized to $R_0^{\mathrm{LiH}} = 1.67$ Å for the neutral ground state, corresponding to an S_0-S_1 excitation energy of 0.1162 a.u. (3.163 eV). We study the dynamics during and after irradiation by a non-perturbative sub-cycle UV pulse that has been previously employed in Ref.[67],

$$\boldsymbol{E}(t) = \boldsymbol{u}E(t) = -\frac{1}{c}\frac{d\boldsymbol{A}(t)}{dt} \tag{8}$$

$$\boldsymbol{A}(t) = \boldsymbol{u}\frac{cE_0}{\omega}\exp\left[-\frac{(t-t_0)^2}{2\sigma^2}\right]\sin(\omega t + \varphi_{\mathrm{CEP}}) \tag{9}$$

with the central frequency, $\omega = 0.127$ a.u. (3.456 eV), roughly tuned to the S_0-S_1 excitation energy, full width half maximum (FWHM) duration of $2\sqrt{2\ln 2}\sigma = 0.85$ fs, temporal offset $t_0 =$ 1.2 fs, field-strength $E_0 = 0.025$ a.u., and carrier-envelope phase (CEP) $\varphi_{\mathrm{CEP}} = \pi$.

The width parameter for the FM decoherence rate, Eq. (5), has been set to the width of the harmonic approximation of the ground-state nuclear wave function in bond-length coordinates, $\sigma = 0.23202$. TSH-FM trajectories have been run for 1000 initial conditions with a nuclear time step of 0.02 fs for a total duration of 90 fs. Four trajectories aborted due to numerical problems, hence 996 trajectories contribute to the ensemble averages.

2.4.2 Glycine

For the glycine molecule, we employed a SA(5)-CASSCF(6,4) approach with the cc-pVDZ basis set, containing one π, one π^*, and two σ orbitals in the active space, which is occupied by six electrons, to optimize the first five electronic states. The equilibrium geometry of the ground state and corresponding normal-mode frequencies were obtained by using second-order many-body perturbation theory (MBPT2). To generate the AXE ensemble of pulse-independent trajectories, all excited states below 10 eV of excitation energy have been considered for a random sample of 1000 initial positions and momenta, resulting in an ensemble of 1979 initial conditions (position, momenta, and active potential) in total, see Sect. 2.3. Therein, usually, the first two electronic excited states were selected. This ensemble of trajectories has been propagated for 15 fs with a 0.3 fs time step. Subsequently, trajectories with a total-energy drift above $\mathscr{E}_D = 0.5$ eV or that crashed were excluded, together with the other trajectories started from the same initial condition, which results in 1852 trajectories in the ensemble for 938 initial positions and momenta. See Ref. 70 for details on the sampling procedure. The PFM decoherence correction scheme is used with the decoherence parameter $\omega_{\mathrm{PFM}} = 4.825 \times 10^{-3}$ a.u., i.e., the geometric mean over the normal-mode frequencies. The electronic dipole matrix elements are evaluated at the nuclear time steps and linearly interpolated for the electronic time steps before evaluating the electronic dipole expectation values to obtain smooth curves.

2.4.3 1,2-dithiane

To simulate the ring-opening dynamics in 1,2-dithiane, involving the S_0, S_1, and S_2 states, we employ a SA(3)-CASSCF(6,4) approach with the 6-31G* basis set, which has been suggested as a simplification[75,76] with respect to earlier work employing a larger active space.[74] The four active orbitals comprise the σ/σ^* pair on the sulfur bond, and the two sulfur lone pair orbitals. The neutral ground state geometry was herein optimized starting from the one obtained with the larger active space in Ref. 74.

Employing a nuclear propagation time-step of 0.5 fs[74–77], we evaluated the TSH dynamics for the PFM decoherence (TSH-PFM)[59], see Sect. 2.1, without decoherence (TSH-ND), and with the widely-used energy-based decoherence correction (TSH-EDC) suggested by Granucci and Persico[45],

$$k_{ia}^{\mathrm{EDC}}(t) = |\mathscr{E}_{ia}(\boldsymbol{R}(t))|\frac{\mathscr{E}_{kin}(\boldsymbol{R}(t))}{\mathscr{E}_{kin}(\boldsymbol{R}(t)) + C} \tag{10}$$

depending only on the kinetic energy, $\mathscr{E}_{kin}(\boldsymbol{R}(t))$, the electronic potential energy difference, $\mathscr{E}_{ia}(\boldsymbol{R}(t))$, and the parameter C, which we set to the recommended value of 0.1 a.u.[42,45] TSH-PFM, TSH-EDC, and TSH-ND simulations of the ring-opening dynamics have been run for 700 fs, starting exclusively from the S_1 excited state, as in previous studies[74–77], as well as when starting from an initial 50:50 superposition of the S_1 and S_2 states, $|\Psi(0)\rangle = \frac{1}{\sqrt{2}}[|\psi_1;\boldsymbol{R}(0)\rangle + |\psi_2;\boldsymbol{R}(0)\rangle]$. In both cases, trajectories with a total energy drift of more than $\mathscr{E}_D = 0.2$ eV have been excluded, resulting in ensembles of 960 (986), 982 (990), and 975 (987) trajectories for simulations of the dynamics following the excitation of the S_1-S_2 coherence (full S_1 excitation) with the TSH-PFM, TSH-EDC, and TSH-ND methods, respectively.

3 Results and discussion

We first analyze the performance of the TSH-FM method with explicit inclusion of the laser field for the dynamics generated in the LiH molecule by a sub-cycle UV pulse. We then showcase the post-processing approach by conducting a systematic study of the dynamics generated in glycine with a series of few-femtosecond UV pulses, scanning bandwidth and central frequency. Finally, we scrutinize the TSH-PFM method for predicting dynamics at long timescales of several 100 fs on the ring opening in 1,2-dithiane and analyze the effect of starting from a superposition of excited electronic states or a single excited state.

To illustrate the evolution of the electronic wave function we depict ensemble-averaged electronic populations and coherences, denoted as diagonal, $\rho_{jj}(t)$, and off-diagonal, $\rho_{jk}(t)$, elements of the density matrix, $\rho_{jk}(t) = \left[\zeta_j(t)\right]^* \zeta_k(t)$, and the components of the electronic dipole, $\boldsymbol{d}(t) = \langle\chi(t)|\hat{\boldsymbol{r}}|\chi(t)\rangle$. Therein, $\zeta_j(t) = c_j(t)$ and $|\chi(t)\rangle = |\Psi(t)\rangle$ for the fully propagated TSH dynamics, see Sections 2.1 and 2.2, and $\zeta_j(t) = C_j(t)$ and $|\chi(t)\rangle = |\Phi(t)\rangle$ for the AXE re-propagated electronic dynamics along pulse-independent trajectories, see Section 2.3.

3.1 Coherent coupled electron-nuclear dynamics in LiH

Herein, we test the combination of TSH-FM[59] with the SHARC approach[65] to incorporate an explicit non-perturbative laser

View Article Online
DOI: 10.1039/D6FD00086J

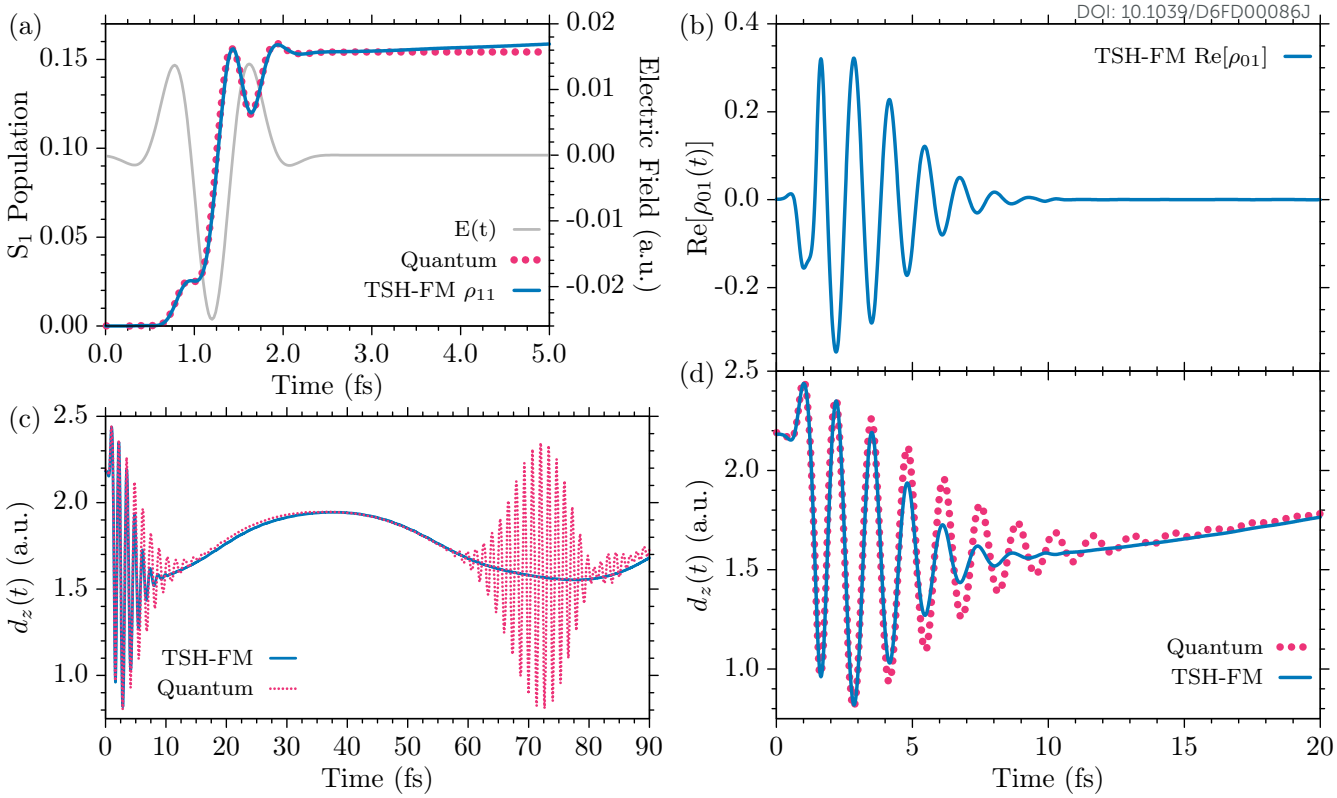

Fig. 1 Dynamics in the LiH model molecule irradiated with a non-perturbative sub-cycle UV laser pulse. (a) Laser field (grey) and adiabatic population of the LiH S_1 electronic state resulting from the TSH-FM simulation (blue) and a full quantum calculation (red, dotted) adapted from Mignolet et al.[67], with permission from AIP Publishing. (b) Evolution of the S_0-S_1 coherence, i.e., the real part of the adiabatic-basis density matrix element, $\mathrm{Re}[\rho_{01}(t)]$, obtained with TSH-FM. (c) Evolution of the LiH electronic dipole along the molecular (z) axis induced by the UV pulse depicted in (a). TSH-FM results (blue) are overlaid with results from a full quantum calculation (red, dotted) adapted from Mignolet et al.[67], with permission from AIP Publishing. (d) Zoom into the first 20 fs of the results shown in panel (c). The TSH-FM results were obtained from an ensemble of 1000 trajectories, see text.

pulse into the simulation, as outlined in Section 2.2. LiH is a well-studied model system for investigating coupled electron-nuclear dynamics driven by non-perturbative lasers with both fully quantum and multiple spawning approaches.[60,61,67–69] We consider a two-state model, involving the S_0 (ground) and S_1 (excited) states of LiH and study the dynamics during and after coherent $S_0 \rightarrow S_1$ excitation by a sub-cycle Gaussian UV pulse, see Eq. (8), with a FWHM duration of 0.85 fs, central frequency of 0.127 a.u. (3.456 eV), and field strength of 0.025 a.u., polarized along the molecular axis, for which quantum-mechanical reference data are available.[67,68]

Figure 1 shows a comparison of our TSH-FM results with the full quantum mechanical ones reported in Ref. 67 for the S_1 population, panel (a), and the z component of the electronic dipole along the molecular axis, panel (c), up to 90 fs. Panel (d) shows a zoom of the first 20 fs to depict the coherent oscillations in more detail. Panel (b) shows the corresponding TSH-FM coherence, represented by $\mathrm{Re}[\rho_{01}(t)]$ in the adiabatic basis. The TSH-FM results have been obtained from an ensemble of 1000 trajectories, out of which 996 contribute to the average, see computational details in Section 2.4.1. In that, the nuclear and electronic dynamics, surface hopping, and decoherence, are evaluated in the field-adiabatic basis, which is equivalent to the adiabatic basis only if the electric field is zero, see Section 2.2. We find that the TSH-FM simulations are internally consistent in the field-adiabatic basis, i.e. the field-adiabatic populations and fraction of active trajectories agree, indicating stability of the approach for the given situation. Moreover, the laser considerably mixes the adiabatic S_0 and S_1 states, so that field-adiabatic and adiabatic populations significantly differ from each other during the presence of the laser, see Appendix A for details. Consequently, we employ the TSH-FM populations in the adiabatic basis to compare against the quantum reference in Fig. 1 (a).

The agreement between TSH-FM and the quantum reference[67] for both the adiabatic populations and the electronic dipole is very good considering the inherent limitations of TSH to classical nuclear dynamics of independent trajectories. In particular, the adiabatic electronic S_1 population, panel (a), excellently matches the quantum result, both during and after the pulse, reaching an asymptotic $S_0 \rightarrow S_1$ excitation probability of 15.5 %. This result confirms the previously reported ability of TSH to accurately predict laser-driven population dynamics for sufficiently short pulses.[62–65] The tiny increase in the TSH-FM population between 3 fs and 5 fs is due to a very slight imperfection in the internal consistency between the adiabatic populations and fraction of active trajectories after the electric field has decayed to zero, with the latter being slightly higher than expected from the adiabatic populations, see Fig. A.1 in Appendix A. This deviation

View Article Online
DOI: 10.1039/D6FD00086J

is in itself a consequence of the stochastic nature of TSH within an ensemble of 1000 trajectories. The observed slight increase in the S_1 population until 5 fs is the compensation of this stochastical deviation in the internal consistency due to decoherence, which moves electronic population to the S_1 state, until internal consistency is perfectly established at 5 fs and kept through the remainder of the propagation.

The S_0-S_1 coherence, panel (b), arises during the pulse, reaches an amplitude of 0.32 after 1.65 fs, which remains for a full period up to 2.85 fs. At later times, i.e., when the pulse is gone, it continues to oscillate with a period of about 1.3 fs with monotonously decreasing amplitude until it vanishes at ∼10 fs as a consequence of the decoherence induced by the decreasing overlap between the wave packets traveling in the S_0 and the much shallower S_1 potential.[67,68] The short-term electronic dipole, panel (d), evaluated with TSH-FM reflects the coherent oscillations with inverted phase, in excellent agreement with the quantum result for the first 3 fs, i.e., during the presence of the pulse. At later times, the coherent oscillations in the electronic dipole predicted with TSH-FM are damped more rapidly than in the quantum result[67], vanishing after about 10 fs, whereas the quantum method predicts sizable oscillations until about 16 fs. However, the non-oscillating, i.e., incoherent, contribution of the electronic dipole, which reflects the nuclear dynamics and the relative populations of the S_0 and S_1 states, is predicted by TSH-FM in very good agreement with the quantum result. This continues to be the case also at longer times until 90 fs, depicted in panel (c). The oscillation with a period of about 78 fs reflects the slow vibration of the molecule in the shallow but bound S_1 potential.[67,68]

As expected, however, TSH-FM is not able to obtain the revival of the coherent oscillation due to the S_1 wave packet returning to the Franck-Condon region of the S_0 state, predicted by the quantum simulation after 60 fs. The reason for this lies at the foundational approximation of TSH being an independent trajectory method[25,26] that is unable to describe neither quantum decoherence nor quantum revivals in the electronic wave function. On the one hand, this can be overcome[67–69] with methods that employ coupled trajectories, such as ab-initio multiple spawning[85,86], or the direct dynamics variational multiconfigurational Gaussian method.[87,88] On the other hand, TSH decoherence corrections, like EDC[45], FM and PFM[59], and many others[37–44,46–55] typically incorporate it by taking into account a strictly positive decoherence rate or probability that allows only for a uni-directional transfer of population towards the active potential, i.e. decoherence. The reversal of this approach, required to describe such a revival, is however, far from trivial.

3.2 Influence of the pulse-generated coherences on coupled electron-nuclear dynamics in glycine

We now use the TSH-PFM decoherence correction scheme in combination with the post-processing approach described in Section 2.3 to perform a systematic study of the coherent dynamics generated by broadband pulses in photo-excited glycine. In contrast to Section 3.1, the nonadiabatic dynamics is propagated here in the absence of any explicit electric field. The action of the external field is instead encoded in the electronic coefficients, $C_j^{(\nu)}(t)$, re-propagated along the trajectory $\boldsymbol{R}^{(\nu)}(t)$, through the initial excitation amplitudes, $C_j^{(\nu)}(0) = c_j^{(\nu)}(0)$, see Sect. 2.3. They are given by first-order perturbation theory,

$$c_j^{(\nu)}(0) = \mathrm{i}\boldsymbol{d}_{j0}(\boldsymbol{R}^{(\nu)}(0)) \cdot \tilde{\boldsymbol{E}}\left(\mathscr{E}_{j0}(\boldsymbol{R}^{(\nu)}(0))\right), \quad \forall j > 0 \qquad (11)$$

in terms of the initial electronic transition dipole moments, $\boldsymbol{d}_{j0}(\boldsymbol{R}^{(\nu)}(0))$, and excitation energies, $\mathscr{E}_{j0}(\boldsymbol{R}^{(\nu)}(0))$, absorbed from the frequency spectrum, $\tilde{\boldsymbol{E}}(\omega)$, of the exciting pump pulse, $\boldsymbol{E}(t)$. The origin of time, $t = 0$, in Eq. (11) is assumed to be the center of the pulse, $\boldsymbol{E}(t)$, in order to render simulations with pulses of different duration comparable. This approximation relies on the assumption that the nuclei are frozen during the short interaction between the molecule and the pulse, so that the phases accumulated by the different electronic states between $t = 0$ and the end of the pulse would only negligibly differ from the ones one would obtain with an explicit inclusion of the field in the computation of the coupled electron-nuclear dynamics.[89,90] Note that we do not include the contribution due to the initial ground state amplitude, $c_0^{(\nu)}(0)$, in the dynamics and (re)-propagate a normalized wave function that at $t = 0$ only includes contributions from the electronic excited states. Explicit trajectory indices, ν, are given since individual trajectory results as well as their averages are discussed in this section.

To define the initial coefficients in Eq. (11), we have used, as in Ref. 70, linearly polarized transform-limited pulses with a real Gaussian spectrum, $\tilde{\boldsymbol{E}}(\omega)$, with central frequency ω_L and FWHM bandwidth $\Delta\omega$. The polarization direction of the electric field, $\boldsymbol{E}(t)$, is $\boldsymbol{e}_z$, normal to the symmetry plane of the molecule, $(\boldsymbol{e}_x, \boldsymbol{e}_y)$. The Gaussian parameters are chosen so as to induce a coherent superposition of the S_1 and S_2 excited electronic states. At the chosen level of theory, the S_1 and S_2 transition energies at the ground state equilibrium geometry are $\mathscr{E}_{10} = 5.79$ eV and $\mathscr{E}_{20} = 9.43$ eV, respectively, with oscillator strengths $f_{01} = 0.00218$ and $f_{02} = 0.02163$. A superposition of the two states can then be excited provided that the central frequency is closer to the darker state S_1 and the bandwidth is large enough to overlap with the brighter state S_2. We thus vary the central frequency, ω_L, between 6.7 eV and 7.7 eV and FWHM bandwidth, $\Delta\omega$, between 2.0 eV and 4.0 eV, corresponding to FWHM durations from 1.29 fs down to 0.65 fs. The set of initial conditions yields 1852 trajectories in total, since most of the time, within the all excited-state ensemble, the two electronic excited states must be considered as the initial active potential for each geometry of the Wigner distribution. The nuclear trajectories and associated matrix elements for the relevant observables (here, the electronic dipole), are calculated once, i.e., in the absence of initial electronic coherences, and setting $c_j^{(\nu)}(0) = \delta_{ja(0)}$ with $a(0)$ the initial active state. The electronic coherences are obtained by re-propagating the electronic TDSE, yielding $C_j^{(\nu)}(t)$, along the pre-computed, frozen trajectories, now with the initial coefficients, $C_j^{(\nu)}(0) = c_j^{(\nu)}(0)$, defined in Eq. (11), for as many as considered pulses, and are a posteriori included into the observable of interest.

In Figure 2, we summarize the results obtained for nine repre-

View Article Online
DOI: 10.1039/D6FD00086J

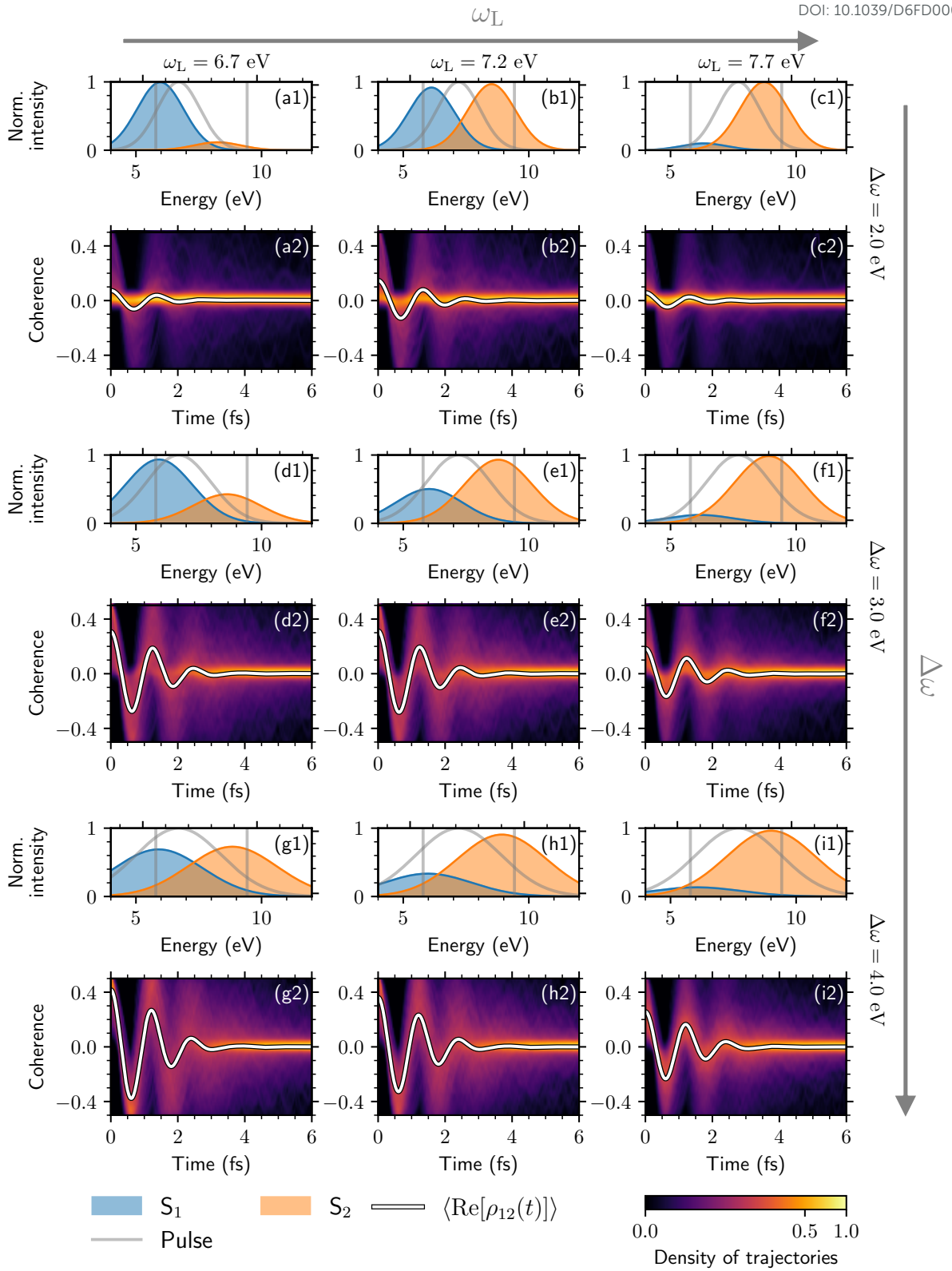

Fig. 2 Coupled electron-nuclear dynamics in glycine excited by nine different UV pulses. Upper sub-panels, (a1) to (i1), initial populations of the S_1 (blue) and S_2 (orange) electronic states of glycine, represented as contributions to the absorption spectrum obtained from first-order perturbation theory using the UV pulses (grey curve) with central frequencies, ω_L, between 6.7 eV and 7.7 eV (along rows), and FWHM bandwidths, $\Delta\omega$, between 2.0 eV and 4.0 eV (along columns). The vertical grey lines indicate the S_1 and S_2 transition energies at the ground-state equilibrium geometry. Lower sub-panels, (a2) to (i2), temporal evolution of the coherence, $\mathrm{Re}[\rho_{12}(t)] = \mathrm{Re}\left[[C_1(t)]^* C_2(t)\right]$, that follows the excitation of the S_1 and S_2 states of glycine by the corresponding UV pulse. Both results for the individual trajectories (through a density of trajectories, using Gaussians with FWHM of 0.05 and a power-law normalization for the color-map with exponent $\Gamma = 1/3$, for visualization purposes) and for the average over all trajectories (thick white line) are displayed. An equivalent figure for the x component of the electronic dipole, $d_x(t)$, is given in Fig. B.1

View Article Online
DOI: 10.1039/D6FD00086J

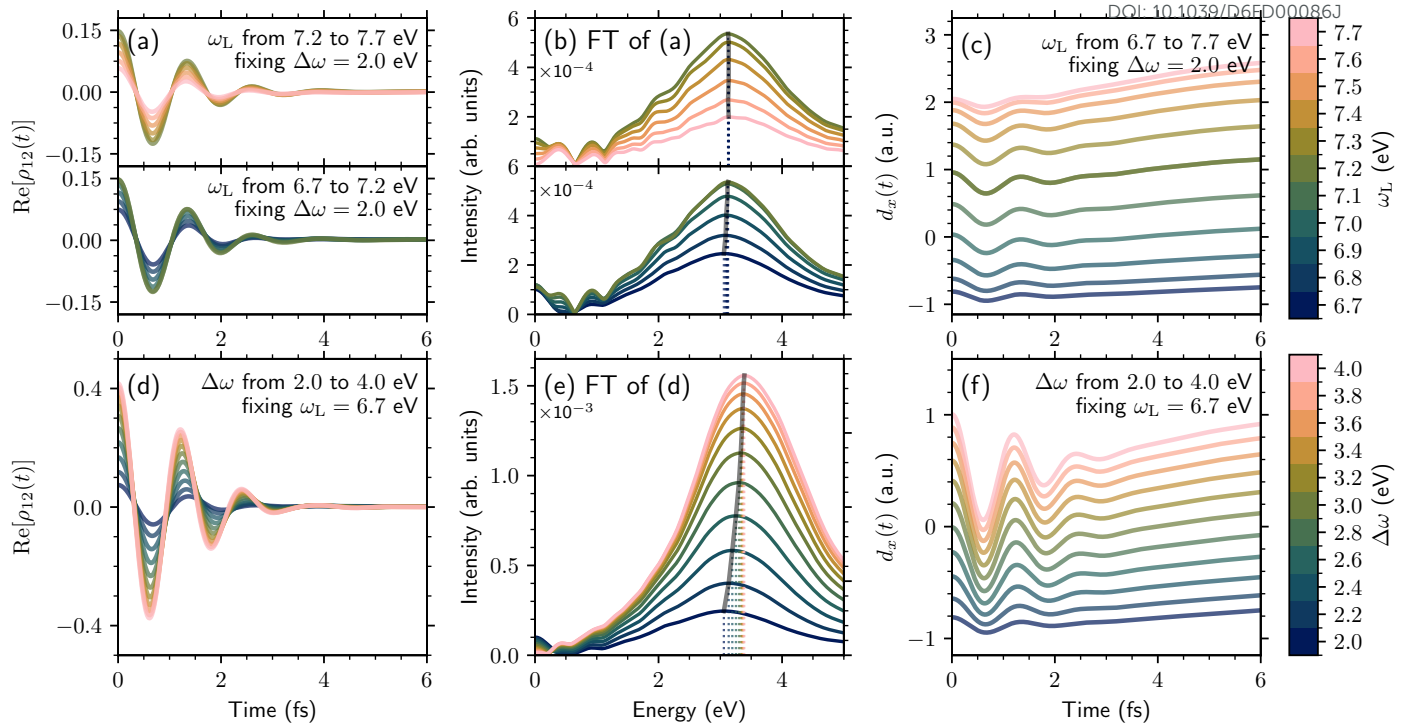

Fig. 3 Average coherence, $\mathrm{Re}[\rho_{12}(t)]$, (a), (d), its Fourier transform (b), (e), and average x component of the electronic dipole, $d_x(t)$, (c), (f), after the excitation of the S_1 and S_2 electronic states of glycine by UV pulses with (a)-(c) fixed FWHM bandwidth, $\Delta\omega = 2.0$ eV, and variable central frequency, ω_L, between 6.7 eV and 7.7 eV (in two separate sub-panels for readability), and (d)-(f) fixed central frequency, $\omega_L = 6.7$ eV, and variable FWHM bandwidth, $\Delta\omega$, between 2.0 eV and 4.0 eV. The gray line in (b), (e) indicates the evolution of the peak of the Fourier transform across the pulses, while the individual peak positions are indicated with vertical dotted lines for every pulse.

sentative cases, varying ω_L (in rows) and $\Delta\omega$ (in columns). The upper sub-panels, (a1) to (i1), display the pulse-generated populations of the S_1 and S_2 states. As can be seen, the considered variations of the pulse parameters allow us to move from scenarios where one of the excited states is dominantly populated, e.g., panels (a1) and (c1), to completely different scenarios where both states are almost equally populated, e.g., panel (g1). The lower sub-panels in Fig. 2, (a2) to (i2), show the calculated coherence, $\mathrm{Re}[\rho_{12}(t)]$, for the whole set of trajectories as a density in time and coherence. It has been obtained by normalizing the weighted sum $f(t,A) = \sum_\nu^{N_t} W^{(\nu)} \gamma(A - A^{(\nu)}(t))$ where $\gamma(A - A^{(\nu)}(t))$ is a fixed-width Gaussian function centered at the expectation value $A^{(\nu)}(t)$ for the trajectory ν. The average over all trajectories is indicated by a thick white line. The coherences oscillate with a period of approximately 1.3 fs, which will be further discussed below, and vanish after a few fs. Increasing the bandwidth of the pulse spectrum from 2.0 to 4.0 eV increases the initial amplitude of the coherences so that they also survive for a longer time.

We now illustrate the capability of our approach to provide observables by using Eq. (6) to compute the evolution of the electronic dipole. The non-zero transition, $j \neq k$, dipole matrix elements, $\boldsymbol{d}_{jk}(\boldsymbol{R}^{(\nu)}(t))$, render the expectation value sensitive to the electronic coherences, $\rho_{jk}^{(\nu)}(t)$, which are thus expected to be reflected in the electronic dipole. The results are shown in Fig. B.1 of Appendix B for the same laser parameters as in Fig. 2. A comparison of the different panels in Fig. B.1 shows that changing the central frequency affects the passive control of the populations, with two different pathways for S_1- and S_2-dominant situations, e.g., Fig. B.1 (a2) to (c2). Increasing the FWHM bandwidth, on the other hand, allows for the excitation of coherent superpositions of states, which exhibit strong oscillatory behaviors between the identified pathways, see, e.g., Fig. B.1 (a2), (d2), and (g2), reflecting the coherences shown in Fig. 2.

The results from the average coherence, its Fourier transform, and the average electronic dipole are summarized in Fig. 3 for systematic scans in pulse central frequency for a bandwidth of 2.0 eV, panels (a), (b), and (c); and in pulse bandwidth for a central frequency of 6.7 eV, panels (d), (e), and (f). When the bandwidth is fixed, Fig. 3 (a) shows a monotonous increase in the amplitude of the resulting coherence for central frequencies varying from 6.7 eV to 7.2 eV and a monotonous decrease when further increasing ω_L from 7.2 eV to 7.7 eV. The distribution of frequencies contributing to the oscillatory behavior of the resulting coherences is mostly unaffected by ω_L, as confirmed by the Fourier transform of the coherence, shown in Fig. 3 (b). The main frequency component stays almost constant, varying in a range from 3.06 eV to 3.14 eV, corresponding to periods of 1.35 fs to 1.32 fs. The evolution of the electronic dipole for the same initial conditions is displayed in Fig. 3 (c). For a fixed pulse bandwidth, the variation of the central frequency, ω_L, mostly affects the population contribution to the average electronic dipole, from negative values for the S_1-dominant situation for $\omega_L \leq 6.9$ eV, to positive values for the S_2-dominant situation at larger ω_L values. Although the coherence is rather small compared to an ideal 50:50 super-

View Article Online
DOI: 10.1039/D6FD00086J

position of states, its contribution is visible in the early dynamics of the electronic dipole, and its amplitude is maximal for pulse central frequencies of about 7.2 eV, see Fig. 3 (c).

For a fixed central frequency of 6.7 eV, closer to the S_1 excitation for narrowband pulses, Fig. 3 (d) shows the effect of the laser bandwidth on the resulting coherences. In particular, increasing the bandwidth from 2.0 eV, corresponding to a duration of 1.29 fs, to 4.0 eV (0.65 fs) tunes the initial population distributions from a situation in which 90% of the population sits in S_1 over a 2:1 S_1:S_2 distribution to an almost equal distribution of populations, for $\Delta\omega = 2.0$, 3.0, and 4.0 eV, respectively. The amplitude of the resulting coherence increases from 0.08 to 0.41, due to the increasing population of the S_2 state with larger bandwidths. Importantly, the frequency spectrum of the coherent oscillations is also affected by the choice of the pulse bandwidth, as highlighted by the Fourier transform of the average coherence, shown in Fig. 3 (e). The peak of the resulting Fourier transform gradually shifts toward larger frequencies, from 3.06 eV to 3.39 eV, corresponding to periods of 1.35 fs and 1.22 fs, respectively. In the mixed quantum-classical picture of TSH, this reflects the fact that pulses with larger bandwidths excite stronger coherences in initial configurations, $R^{(\nu)}(0)$, of the glycine molecule that have a larger initial S_1-S_2 potential-energy gap, $\mathscr{E}_{21}(\boldsymbol{R}^{(\nu)}(0))$. The electronic dipole shown in Fig. 3 (f) displays a clear change in both the population and coherence contributions, reflected in the slowly-varying background and the oscillating contribution visible for about 3 fs, respectively. Here, the variation due to the population is not as strong as when varying the central frequency because, as pointed out above, only situations between a mainly S_1-populated initial state, on the one hand, and an about 50:50 S_1:S_2 population distribution, on the other hand, are covered by scanning the bandwidth from 2.0 to 4.0 eV at a central frequency of 6.7 eV, see panels (a1), (d1), and (g1) in Figs. 2 and B.1. At the same time, the oscillations featured in the electronic dipole and the increase of their amplitude for larger pulse bandwidths reflect the electronic coherences and thus the same behavior as that displayed in Fig. 2.

Even if some of these findings could have been expected, they indicate that performing calculations with TSH-PFM in combination with the post-processing method described above allows one to model the coupled electron-nuclear dynamics arising from hundreds of different pulses and, when required, the observables of interest for a price that is only slightly higher than that required for a single pulse. Such a capability also opens the way to the theoretical investigations of control strategies, aimed at manipulating the outcome of molecular excitation by directly acting on the superposition of the electronic excited states.

3.3 Dynamics in 1,2-dithiane starting from a coherent superposition of electronic states

The ring-opening and ring-closing dynamics in 1,2-dithiane represents a well-known model system for strongly nonadiabatic dynamics as the potentials of the ground, S_0, and excited states, S_1, S_2, become degenerate and strongly coupled as the sulfur-sulfur bond opens up and the molecule assumes an elongated structure,

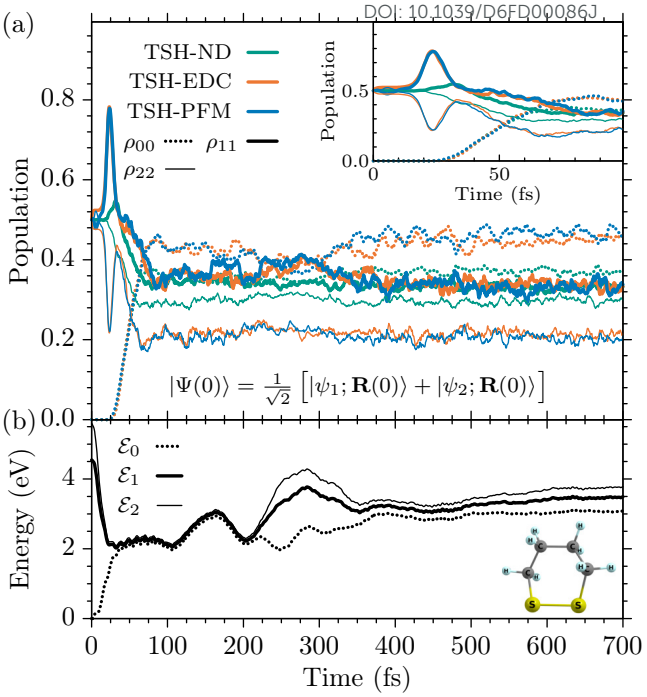

Fig. 4 Nonadiabatic dynamics of 1,2-dithiane induced by a symmetric superposition of the S_1 and S_2 electronic excited states, $|\Psi(0)\rangle = \frac{1}{\sqrt{2}}[|\psi_1;\boldsymbol{R}(0)\rangle + |\psi_2;\boldsymbol{R}(0)\rangle]$. (a) Adiabatic populations of the S_0 ($\rho_{00}(t)$, dotted), S_1 ($\rho_{11}(t)$, thick), and S_2 ($\rho_{22}(t)$, thin) states obtained with TSH-ND (turquoise), TSH-EDC (orange), and TSH-PFM (blue), for respective ensembles of 1000 trajectories, see text. (b) Ensemble-averaged adiabatic potential energies of the S_0 ($\mathscr{E}_0$, dotted), S_1 ($\mathscr{E}_1$, thick), and S_2 ($\mathscr{E}_2$, thin) electronic states obtained with TSH-PFM.

before closing the ring again after about 310 fs.[74–77] It thus provides and ideal test bed for the TSH-PFM method, which has not yet been applied to describe the coupled electron-nuclear dynamics involving complicated structural rearrangements at such long time scales.

To investigate the potential effect of initial coherences on the ring-opening dynamics in the 1,2-dithiane molecule, we have considered a 50:50 S_1-S_2 coherent superposition, $|\boldsymbol{\Psi}(0)\rangle = \frac{1}{\sqrt{2}}[|\psi_1;\boldsymbol{R}(0)\rangle + |\psi_2;\boldsymbol{R}(0)\rangle]$, and applied the TSH-PFM methodology to describe the ensuing coupled electron-nuclear dynamics. Further, we compare these results to those obtained without decoherence correction (TSH-ND), and with those obtained by including the widely employed energy-based decoherence correction[45] (TSH-EDC). In all three cases, we run trajectories starting from 1000 initial conditions sampled from the ground-state Wigner distribution, out of which 982 (TSH-EDC), 960 (TSH-PFM), and 975 (TSH-ND) are taken into account in the ensemble averages presented herein, see computational details in Section 2.4.3. Figure 4 shows the evolution of the S_0, S_1, and S_2 adiabatic electronic populations, panel (a), and energies, panel (b). Both TSH-PFM and TSH-EDC predict essentially the same population dynamics. It starts with a sudden increase of the S_1 population from its initial value of 0.5 to 0.78 after 24 fs, followed by a rapid decrease up to 34 fs. This is followed by a decrease in both the S_1 and S_2 populations to about 0.36 and 0.2, respectively, at around 80fs, while, from 25 fs onwards, the remaining portion of about 0.44

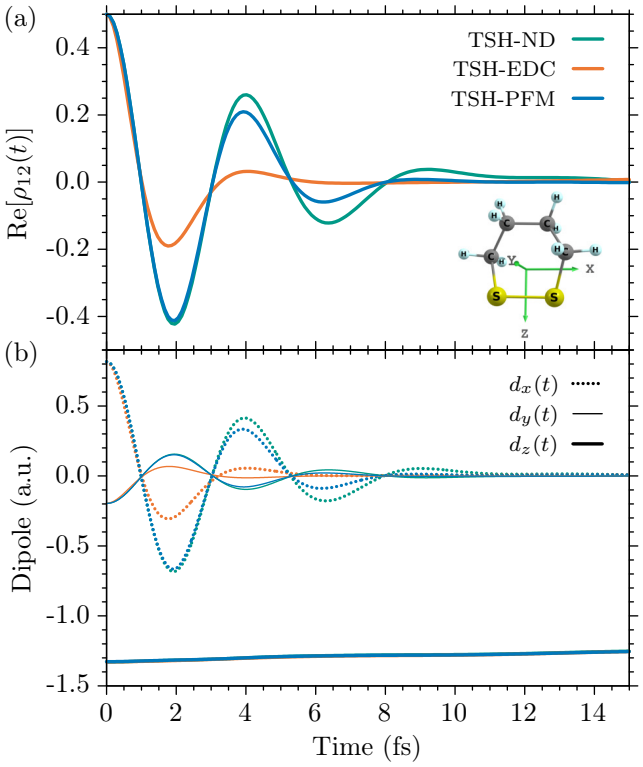

Fig. 5 Short-time dynamics in 1,2-dithiane driven by the initial S_1-S_2 excited-state coherent superposition, $|\Psi(0)\rangle = \frac{1}{\sqrt{2}}[|\psi_1;\boldsymbol{R}(0)\rangle + |\psi_2;\boldsymbol{R}(0)\rangle]$, obtained with TSH-ND (turquoise), TSH-EDC (orange), and TSH-PFM (blue), for respective ensembles of 1000 trajectories, see text. (a) Evolution of the coherence represented by the off-diagonal density matrix element, $\mathrm{Re}[\rho_{12}(t)]$. (b) x (dotted), y (thin), and z (thick) components of the electronic dipole vector. Coordinate axes are defined in the inset in (a).

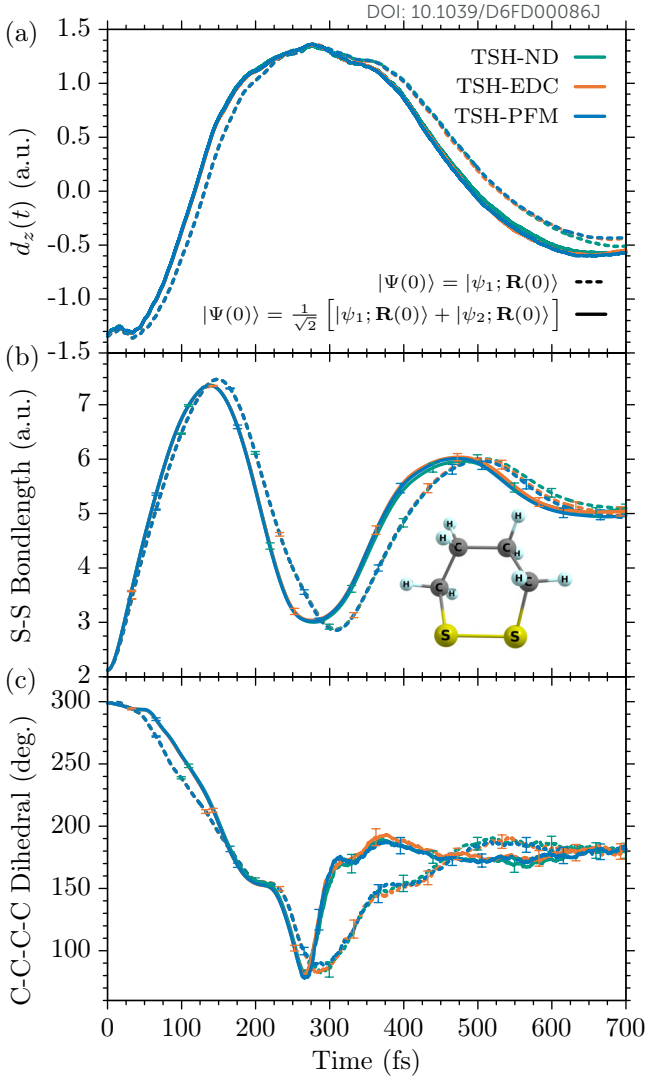

Fig. 6 Nonadiabatic ring-opening dynamics of 1,2-dithiane induced by an initial S_1 excitation (dashed curves) and by a coherent superposition of the S_1 and S_2 states, $|\Psi(0)\rangle = \frac{1}{\sqrt{2}}[|\psi_1;\boldsymbol{R}(0)\rangle + |\psi_2;\boldsymbol{R}(0)\rangle]$ (solid curves), obtained with TSH-ND (turquoise), TSH-EDC (orange), and TSH-PFM (blue), for respective ensembles of 1000 trajectories, see text. (a) z component of the electronic dipole vector. The x and y components are zero after the decay of the initial coherence, see Fig. 5, and not shown. (b) Sulfur-sulfur distance. (c) C-C-C-C dihedral angle. The error bars correspond to the 95% confidence intervals of the ensemble averages.

goes to the ground state S_0. This dynamics is the consequence of nonadiabatic transitions between these states, as their adiabatic potential energies become nearly degenerate after 25 fs, see panel (b). The potential energies become non-degenerate again between about 225 fs and 355 fs, corresponding to the time during which the ring closes again for the first time, see Fig. 6. Note that during this time, the S_0 and S_1 populations predicted by TSH-PFM and TSH-EDC approach each other and even flip with values around 0.39 between about 250 fs and 305 fs, while they separate again at later times, weakly oscillating around their asymptotic values of 0.34 (S_1) and 0.46 (S_0). The S_2 population stays close to 0.2 for the whole propagation after the first 80 fs. TSH-ND, without decoherence, predicts different population dynamics. It misses the abrupt changes in the populations of the S_1 and S_2 states up to 34 fs and, after 80 fs, predicts S_0 and S_2 populations around 0.36 and 0.30, i.e., significantly lower (S_0) and higher values (S_2) than obtained with TSH-PFM and TSH-EDC, respectively.

It is important to note that the TSH-PFM and TSH-EDC calculations are internally consistent, i.e., the adiabatic electronic populations match the fractions of active trajectories propagating in S_0, S_1, and S_2, indicating long-term stability of the TSH-PFM approach for such dynamics, while this is not the case for the TSH-ND approach, see the SI. Further, the population dynamics obtained from the initial S_1-S_2 coherence after 80 fs approximately matches the one obtained when launching the dynamics from the S_1 potential, as in previous studies[74–77], see Appendix C.

Figure 5 shows the short-time evolution of the S_1-S_2 coherence, $\mathrm{Re}[\rho_{12}(t)]$, in panel (a) and the electronic dipole, panel (b), along the x, y, z directions defined in the inset of panel (a) for TSH-PFM, TSH-EDC, and TSH-ND. TSH-PFM predicts that electronic coherence survives up to ~10 fs, only slightly shorter than the TSH-ND result, i.e., the maximum coherence in independent-trajectory TSH simulations, but significantly longer than the TSH-EDC prediction. In the latter case, the coherence vanishes already around 5 fs. Similar discrepancies have been reported for neutral glycine

View Article Online
DOI: 10.1039/D6FD00086J

and the modified bismethyl-adamantane (BMA[5,5]), and para-xylene cations[59], although quantum-mechanical calculations[22] predict longer-lived coherences than either TSH approach for the latter two cases.

For all three methods, the x and y components of the electronic dipole oscillate around zero, reflecting the progressive decay of the coherence, while the z component remains constant at -1.3 a.u., as shown in Fig. 5 (b). In that, the amplitudes of the x component, along the sulfur bond, are largest and in phase with the coherence shown in panel (a), while the y component, perpendicular to the molecular plane, oscillates with the opposite phase at smaller amplitudes. The fact that the z component is constant reflects that, along this direction, the S_1-S_2 transition dipole is zero in our calculations, while the permanent S_0, S_1, and S_2 dipoles dominate. The opposite is true for the x and y components, where only the S_1-S_2 transition dipole contributes. At long times it is thus sufficient to analyze the z component of the dipole.

Figure 6 shows the evolution of the z component of the electronic dipole, panel (a), the sulfur-sulfur distance, panel (b), and the C-C-C-C dihedral angle, panel (c), resulting from starting the dynamics in the S_1-S_2 coherent superposition, as well as in the S_1 state, as considered in previous works[74–77], for TSH-PFM, TSH-EDC, and TSH-ND. In spite of the differences between the three methods in describing the evolution of the populations and coherences, they predict nearly identical structural dynamics in 1,2-dithiane for both initial conditions. This is because TSH-ND, besides being internally inconsistent, predicts similar fractions of active trajectories propagating in the S_0, S_1, and S_2 states as TSH-PFM and TSH-EDC, see the SI for details. Hence, all properties that exclusively depend on the nuclear motion are predicted in nearly the same manner by all methods, although there are considerable differences in properties sensitive to the electronic wave functions.

The first ring opening is visualized by the inter-sulfur distance. It increases from the equilibrium value of about 2.1 a.u. to 7.3 a.u. at around 137 fs if starting from the S_1-S_2 coherent superposition, and to 7.5 a.u. at 150 fs, if starting exclusively from the S_1 state. In parallel, the respective C-C-C-C dihedral angle decreases from 300° down to 220°, for the initial coherence, and to 195°, when starting in the S_1 potential. Beyond the respective times of maximum ring opening, the inter-sulfur distance decreases again, restoring the ring shape after 275 fs for the initial S_1-S_2 coherence and after 310 fs when starting from the S_1 state. The C-C-C-C dihedral angle further decreases to around 80° after 265 fs for the initial coherence and to 85° after 288 fs when starting from the S_1 state, i.e., about 10 fs and 20 fs before the minimum inter-sulfur distance is respectively reached. The fact that the dihedral angle does not return to about 300°, but further decreases as the intersulfur distance decreases again, indicates that the ring closes on the opposite site of the molecule before opening again, in analogy to 'Newtons cradle'.[74] The same conclusion can be drawn from the electronic z-dipole, panel (a), which changes its sign over a full period of the ring opening and requires two periods to restore the original negative sign. With the onset of the second ring opening, the dihedral angle increases much more rapidly, within 45 fs to a small plateau at about 170°, for the dynamics started from the coherence, whereas this happens more slowly, within about 75 fs and reaching just about 150°, for the dynamics starting from the S_1 state. At longer times, the oscillations in the inter-sulfur distance are progressively damped, since an increasing number of trajectories cease to continue the 'Newtons-cradle' sequence of ring-opening and ring-closing.[74] This effect is even more apparent in the dihedral angle. The differences between the dynamics started from the S_1-S_2 coherence and from only the S_1 potential slightly increase with time, as can be seen in the electronic dipole and the inter-sulfur distance, although the progressive damping reduces this characteristic after about 500 fs.

These results underline that, although the initial electronic coherence does not survive beyond 10 fs, the simultaneous population of two excited states by a broadband pulse can affect the long-term structural dynamics in a molecule. The reason for this is the different inclination of the S_1 and S_2 potential surfaces, due to which the trajectories initialized at $t = 0$ in the S_2 potential accumulate more kinetic energy and hence exhibit a faster dynamics, see Fig. 4 (b).

4 Conclusions

We have shown that the one-dimensional variant of the trajectory surface hopping with projected forces and momenta (TSH-PFM) method[59] in combination with the surface hopping including arbitrary couplings (SHARC) approach[65] allows one to describe the coherent electron dynamics during and after interaction of the LiH molecule with a non-perturbative sub-cycle UV pulse in good agreement with the results of full quantum calculations as long as quantum revivals do not occur. We have also showcased how the combination of a recently proposed post-processing approach[70] with the TSH-PFM method allows exploring potential control schemes in glycine based on manipulating the initial electronic coherences and populations with different perturbative few-femtosecond UV pulses. The method allows for a gradual tuning of the degree of electronic coherence and their survival time by varying the pulse central frequency and bandwidth at low computational cost, as only the electronic dynamics is re-evaluated in each case. Finally we have shown for the ring-opening dynamics in 1,2-dithiane that the TSH-PFM method yields exactly the same structural dynamics at long times (several 100 fs) as predicted by well established TSH approaches. Interestingly, in this case, we have found that the population distribution created by a coherent excitation can affect long-term structural dynamics with respect to exciting only a single electronic state. All this suggests that the use of tunable few-femtosecond UV pulses to coherently excite several electronic states in neutral molecules can open promising paths to induce unusual chemical behaviors, one of the main goals of attochemistry.

Appendix

A Lithium hydride: Internal consistency

An ensemble of TSH trajectories is internally consistent if the average over the electronic populations of the individual trajectories, $\rho_{jj}(t)$, agrees with the respective fraction of active trajecto-

View Article Online
DOI: 10.1039/D6FD00086J

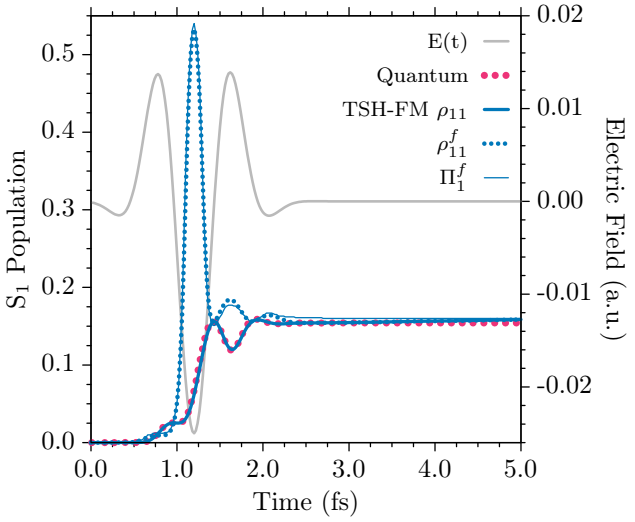

Fig. A.1 LiH S_1 population induced by irradiation with the sub-cycle UV pulse (grey) employed in the main text, see Fig 1 (a). The full quantum result (red large dots) adapted from Mignolet et al.[67], with permission from AIP Publishing, is shown together with the TSH-FM results for the S_1 populations in the adiabatic basis ($\rho_{11}(t)$, thick blue), the field-adiabatic basis ($\rho^f_{11}(t)$, dotted blue), and with the fraction of active trajectories propagating in the field-adiabatic S_1 potential ($\Pi^f_1(t)$, thin blue), see text. The TSH-FM results have been obtained from an ensemble of 1000 trajectories.

ries, $\Pi_j(t)$[40],

$$\overbrace{\frac{1}{N_t}\sum_{\nu=1}^{N_t}|c_j^{(\nu)}(t)|^2}^{\rho_{jj}(t)} \approx \overbrace{\frac{N_j(t)}{N_t}}^{\Pi_j(t)} \tag{A.1}$$

where $N_j(t)$ is the number of trajectories, $\boldsymbol{R}^{(\nu)}(t)$, that propagate at time t along the electronic potential surface $\mathscr{E}_j(\boldsymbol{R})$. Within the SHARC approach, a laser couples the adiabatic potentials, introducing the field-adiabatic basis that coincides with the adiabatic basis in absence of the field[65], as discussed in Sect. 2.2. Since the dynamics is calculated in the field-adiabatic basis, Fig. A.1 compares the TSH-FM field-adiabatic S_1 populations, $\rho^f_{11}(t)$, and the fraction of active trajectories propagating in the field-adiabatic S_1 state, $\Pi^f_1(t)$, for the ensemble of trajectories utilized in the main text, Sect. 3.1. Indeed, both quantities agree almost perfectly in the presence of the pulse and at later times, demonstrating that TSH-FM is internally consistent in both situations. To visualize the degree of state-mixing induced by the laser, the field-free adiabatic-basis, $\rho_{11}(t)$, resulting from TSH-FM and the full quantum mechanical calculations from Ref. 67, depicted also in Fig. 1 of the main text, are given here as well. The slight internal inconsistency of less than 1% that occurs just after the pulse has decayed to zero at around 2.5 fs is the consequence of the stochastic surface hopping process over an ensemble of 1000 trajectories. It could be reduced further by employing a larger number of trajectories, although this would not significantly affect the quantities shown in Fig. 1.

B Glycine's electronic dipoles

For the same nine cases shown in Fig. 2, we display in Fig B.1 the x component of the electronic dipole, which we use to decipher the contributions of populations and coherences in the observable. In the upper row of Fig B.1, (a2) to (c2), we clearly observe that the variation of the central frequency from 6.7 eV to 7.7 eV passively controls the selection of either only the state S_1, a superposition of the states S_1 and S_2, or only the state S_2. The intermediate case with a superposition of the two states already exhibits some oscillatory behavior at the beginning, which is due to the non-negligible initial coherence, see Fig. 2. Changing the FWHM bandwidth of the pulse as, e.g., in the first column of Fig. B.1, (a2), (d2), and (g2) allows control of the population (from only S_1 to a superposition of S_1 and S_2) but, most importantly, it increases the initial coherence between the two states, as was previously shown in Fig. 2. Due to the non-vanishing transition dipole moment between the two states, $\boldsymbol{d}_{12}(\boldsymbol{R}^{(\nu)}(t))$, in Eq. (6), the early dynamics of the electronic dipole reflects the strong initial S_1-S_2 coherence. The other, second and third, columns show similar results, with the only difference being that the S_2 state is now more dominant, panels (e2), (f2), (h2), and (i2), due to the central frequency, ω_L, being shifted towards the transition energy of S_2.

C S_1-excited ring-opening of 1,2-dithiane

The 1,2-dithiane population dynamics and potential energies following an initial S_1 excitation, which has been the subject of previous studies[74–77], are depicted in Fig. C.1. It complements Fig. 4 for the initial 50:50 S_1-S_2 coherent superposition of states and corresponds to the electronic dipole and structural dynamics shown in Fig. 6. Panel (a) depicts the adiabatic electronic populations of the ground, S_0, and excited, S_1, S_2, states obtained with the TSH-PFM, TSH-EDC, and TSH-ND methods; panel (b) shows the respective TSH-PFM potential energies. As in Fig. 4, the TSH-PFM and TSH-EDC adiabatic electronic populations evolve very similar, first predicting a drop of the S_1 population to about 0.48, while the S_2 population increases to roughly 0.52 within about 32 fs. Subsequently, the ground-state, S_0, starts acquiring population, after the potential energies of the S_0, S_1, and S_2 states have become degenerate, and supersedes the excited states at about 70 fs. After about 80 fs, the populations have stabilized at about 0.45, S_0, 0.35, S_1, and 0.2, S_2, until the ring closes again between about 255 fs and 355 fs, due to which the potential energies again become non-degenerate, see panel (b), and the S_0 and S_1 populations approach each other. At later times, the populations adopt asymptotic values of 0.48, S_0, 0.32, S_1, and 0.2, S_2. TSH-ND predicts a stronger transient S_1-S_2 population transfer, peaking at 0.60 S_2 population after 32 fs, as well as asymptotic S_0 and S_2 populations of 0.38 and 0.30, respectively, notably lower and higher than the corresponding TSH-PFM and TSH-EDC results. In comparison to the dynamics following the S_1-S_2 coherent superposition, see Fig. 4, the S_1-excited population dynamics appears similar, though not exactly the same after the first 50 fs. Further, the adiabatic potentials become non-degenerate around

View Article Online
DOI: 10.1039/D6FD00086J

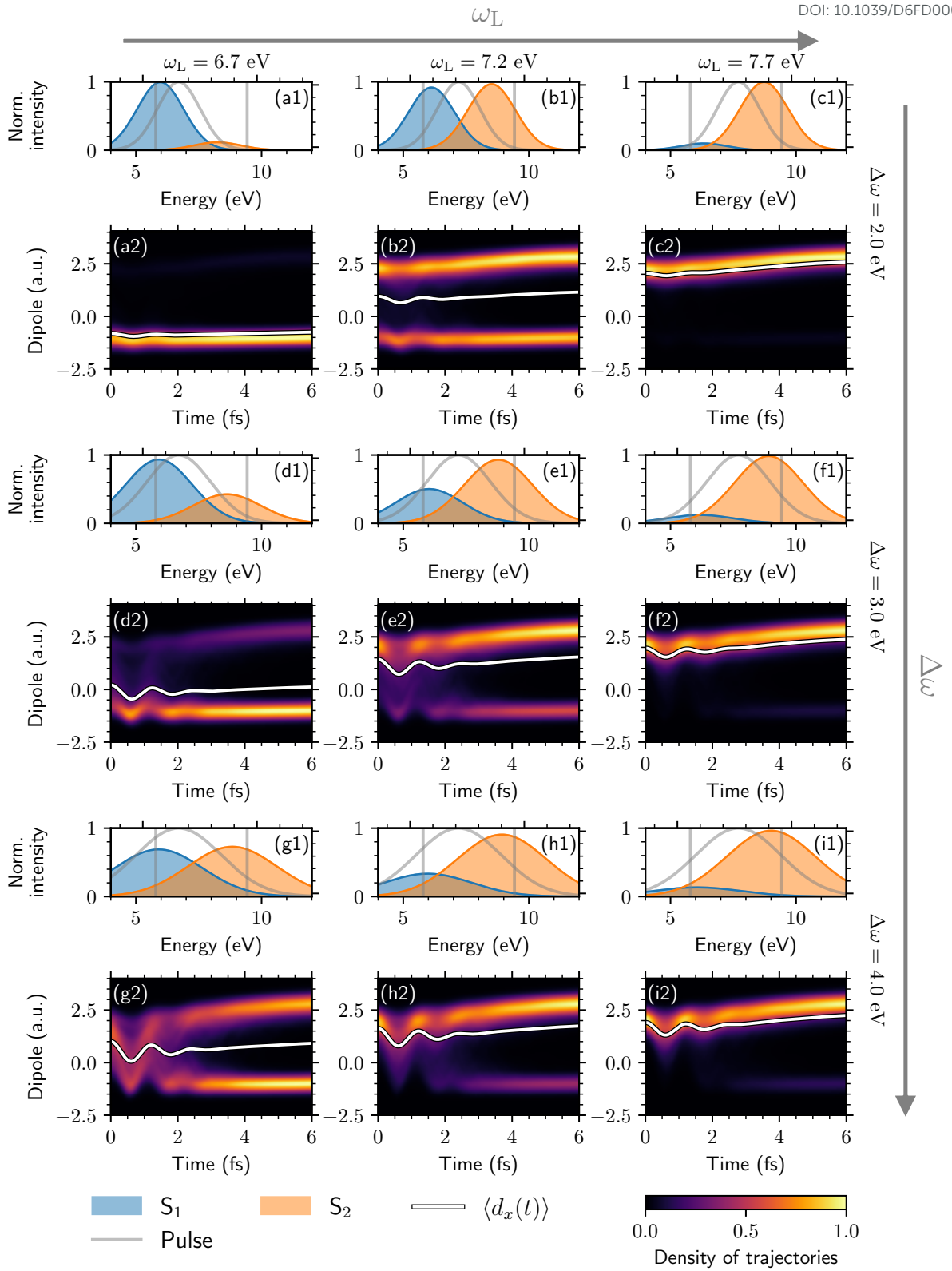

Fig. B.1 Same as Fig. 2, but for the temporal evolution of the x component of the electronic dipole, $d_x(t)$. The FWHM of the Gaussian used for the density of trajectories is 0.5 a.u.

30 fs later in the S_1-excited case, in accord with the observation that the initial S_2 population, accelerates the ring-opening, since the corresponding trajectories acquire more kinetic energy from the steeper S_2 potential, see also Fig 6.

View Article Online
DOI: 10.1039/D6FD00086J

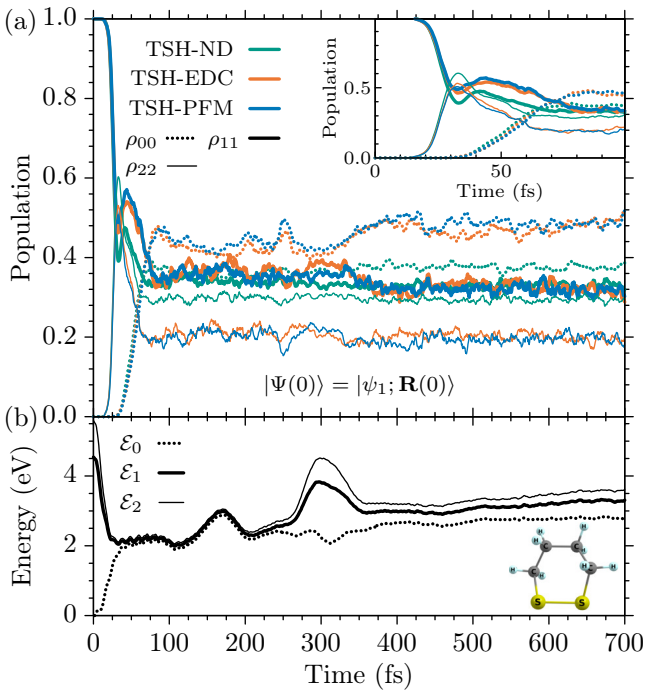

Fig. C.1 Same as Fig. 4, but for starting the dynamics from an initial S_1 excitation, $|\Psi(0)\rangle = |\psi_1; \boldsymbol{R}(0)\rangle$. All TSH results have been obtained for respective ensembles of 1000 trajectories, see the main text.

Data availability

The data supporting this article have been included as part of the Supplementary Information (SI): (i) additional explanations of the inactive-potential momentum propagation for the FM decoherence correction in presence of a laser field; (ii) additional figures and analysis for the ring-opening and ring-closing dynamics in the 1,2-dithiane molecule; (iii) the optimized ground-state geometries and harmonic frequencies used to build the Wigner distribution for all molecules. See DOI: XXXXXXXX.

Conflicts of interest

There are no conflicts to declare.

Acknowledgements

This work has been supported by the European Research Council (ERC) under the European Union Horizon 2020 research and innovation programme (grant agreement no. 951224, TOMATTO), the Ministerio de Ciencia e Innovación MICINN (Spain) through the projects PID2022-138288NB-C31 and PID2022-138288NB-C32, the "Severo Ochoa" Programme for Centres of Excellence in R&D (CEX2020-001039-S) and the "María de Maeztu" Programme for Units of Excellence in R&D (CEX2018-000805-M), and the regional government of Madrid (Spain) through the Tecnologías 2024 program, project MATRIX-CM (Grant No. TEC-2024/TEC-85). S.M.C. acknowledges support from the Ramón y Cajal program (RYC2023-044186-I) financed by MICIU/AEI/10.13039/501100011033 and the FSE+. All calculations were performed at the Mare Nostrum Supercomputer of the Red Española de Supercomputación (BSC-RES) and the Centro de Computación Científica de la Universidad Autónoma de Madrid (CCC-UAM).

Notes and references

1 G. Sansone, E. Benedetti, F. Calegari, C. Vozzi, L. Avaldi, R. Flammini, L. Poletto, P. Villoresi, C. Altucci, R. Velotta, S. Stagira, S. De Silvestri and M. Nisoli, *Science*, 2006, **314**, 443–446.

2 F. Krausz and M. Ivanov, *Rev. Mod. Phys.*, 2009, **81**, 163–234.

3 F. Calegari, G. Sansone, S. Stagira, C. Vozzi and M. Nisoli, *J. Phys. B: At., Mol. Opt. Phys.*, 2016, **49**, 062001.

4 C. Pellegrini, A. Marinelli and S. Reiche, *Rev. Mod. Phys.*, 2016, **88**, 015006.

5 L. S. Cederbaum and J. Zobeley, *Chem. Phys. Lett.*, 1999, **307**, 205–210.

6 G. Sansone, F. Kelkensberg, J. F. Pérez-Torres, F. Morales, M. F. Kling, W. Siu, O. Ghafur, P. Johnsson, M. Swoboda, E. Benedetti, F. Ferrari, F. Lépine, J. L. Sanz-Vicario, S. Zherebtsov, I. Znakovskaya, A. L'Huillier, M. Y. Ivanov, M. Nisoli, F. Martín and M. J. J. Vrakking, *Nature*, 2010, **465**, 763–766.

7 F. Calegari, D. Ayuso, A. Trabattoni, L. Belshaw, S. De Camillis, S. Anumula, F. Frassetto, L. Poletto, A. Palacios, P. Decleva, J. B. Greenwood, F. Martín and M. Nisoli, *Science*, 2014, **346**, 336–339.

8 P. M. Kraus, B. Mignolet, D. Baykusheva, A. Rupenyan, L. Horný, E. F. Penka, G. Grassi, O. I. Tolstikhin, J. Schneider, F. Jensen, L. B. Madsen, A. D. Bandrauk, F. Remacle and H. J. Wörner, *Science*, 2015, **350**, 790–795.

9 M. Lara-Astiaso, A. Palacios, P. Decleva, I. Tavernelli and F. Martín, *Chem. Phys. Lett.*, 2017, **683**, 357–364.

10 D. Schwickert, M. Ruberti, P. Kolorenč, S. Usenko, A. Przystawik, K. Baev, I. Baev, M. Braune, L. Bocklage, M. K. Czwalinna, S. Deinert, S. Düsterer, A. Hans, G. Hartmann, C. Haunhorst, M. Kuhlmann, S. Palutke, R. Röhlsberger, J. Rönsch-Schulenburg, P. Schmidt, S. Toleikis, J. Viefhaus, M. Martins, A. Knie, D. Kip, V. Averbukh, J. P. Marangos and T. Laarmann, *Sci. Adv.*, 2022, **8**, eabn6848.

11 Y. Kobayashi and S. R. Leone, *J. Chem. Phys.*, 2022, **157**, 180901.

12 F. Vismarra, F. Fernández-Villoria, D. Mocci, J. González-Vázquez, Y. Wu, L. Colaizzi, F. Holzmeier, J. Delgado, J. Santos, L. Bañares, L. Carlini, M. C. Castrovilli, P. Bolognesi, R. Richter, L. Avaldi, A. Palacios, M. Lucchini, M. Reduzzi, R. Borrego-Varillas, N. Martín, F. Martín and M. Nisoli, *Nat. Chem.*, 2024, **16**, 2017–2024.

13 M. Galli, V. Wanie, D. P. Lopes, E. P. Månsson, A. Trabattoni, L. Colaizzi, K. Saraswathula, A. Cartella, F. Frassetto, L. Poletto, F. Légaré, S. Stagira, M. Nisoli, R. Martínez Vázquez, R. Osellame and F. Calegari, *Opt. Lett.*, 2019, **44**, 1308–1311.

14 M. Reduzzi, M. Pini, L. Mai, F. Cappenberg, L. Colaizzi, F. Vismarra, A. Crego, M. Lucchini, C. Brahms, J. C. Travers, R. Borrego-Varillas and M. Nisoli, *Opt. Express*, 2023, **31**, 26854–26864.

15 L. Colaizzi, S. Ryabchuk, E. P. Månsson, K. Saraswathula,

V. Wanie, A. Trabattoni, J. González-Vázquez, F. Martín and F. Calegari, *Nat. Commun.*, 2024, **15**, 9196.
16 V. Wanie, E. Bloch, E. P. Månsson, L. Colaizzi, S. Ryabchuk, K. Saraswathula, A. F. Ordonez, D. Ayuso, O. Smirnova, A. Trabattoni, V. Blanchet, N. Ben Amor, M.-C. Heitz, Y. Mairesse, B. Pons and F. Calegari, *Nature*, 2024, **630**, 109–115.
17 A. M. Heinzerling, F. Tani, M. Agarwal, V. S. Yakovlev, F. Krausz and N. Karpowicz, *Nat. Photonics*, 2025, **19**, 772–777.
18 M. Nisoli, P. Decleva, F. Calegari, A. Palacios and F. Martín, *Chem. Rev.*, 2017, **117**, 10760–10825.
19 I. C. D. Merritt, D. Jacquemin and M. Vacher, *J. Phys. Chem. Lett.*, 2021, **12**, 8404–8415.
20 F. Calegari and F. Martín, *Commun. Chem.*, 2023, **6**, 184.
21 F. Martín, F. Calegari, C. Vozzi, K. Ueda and L. DiMauro, *J. Phys. Chem. A*, 2024, **128**, 4761–4764.
22 M. Vacher, M. J. Bearpark, M. A. Robb and J. P. Malhado, *Phys. Rev. Lett.*, 2017, **118**, 083001.
23 L. Fransén, S. Gómez and M. Vacher, *J. Phys. Chem. Lett.*, 2025, **16**, 8745–8751.
24 *Quantum Chemistry and Dynamics of Excited States: Methods and Applications*, ed. L. González and R. Lindh, John Wiley & Sons Ltd., 2021.
25 J. C. Tully and R. K. Preston, *J. Chem. Phys.*, 1971, **55**, 562–572.
26 J. C. Tully, *J. Chem. Phys.*, 1990, **93**, 1061–1071.
27 J. C. Tully, *Faraday Discuss.*, 1998, **110**, 407–419.
28 A. W. Jasper, S. Nangia, C. Zhu and D. G. Truhlar, *Acc. Chem. Res.*, 2006, **39**, 101–108.
29 M. Barbatti, *Wiley Interdiscip. Rev.: Comput. Mol. Sci.*, 2011, **1**, 620–633.
30 J. C. Tully, *J. Chem. Phys.*, 2012, **137**, 22A301.
31 L. Wang, A. Akimov and O. V. Prezhdo, *J. Phys. Chem. Lett.*, 2016, **7**, 2100–2112.
32 R. Crespo-Otero and M. Barbatti, *Chem. Rev.*, 2018, **118**, 7026–7068.
33 L. Wang, J. Qiu, X. Bai and J. Xu, *Wiley Interdiscip. Rev.: Comput. Mol. Sci.*, 2020, **10**, e1435.
34 T. R. Nelson, A. J. White, J. A. Bjorgaard, A. E. Sifain, Y. Zhang, B. Nebgen, S. Fernandez-Alberti, D. Mozyrsky, A. E. Roitberg and S. Tretiak, *Chem. Rev.*, 2020, **120**, 2215–2287.
35 S. Mai, P. Marquetand and L. González, in *Quantum Chemistry and Dynamics of Excited States: Methods and Applications*, ed. L. González and R. Lindh, John Wiley & Sons Ltd., 1st edn., 2020, pp. 499–530.
36 A. Jain and A. Sindhu, *ACS Omega*, 2022, **7**, 45810–45824.
37 E. Neria and A. Nitzan, *J. Chem. Phys.*, 1993, **99**, 1109–1123.
38 S. Hammes-Schiffer and J. C. Tully, *J. Chem. Phys.*, 1994, **101**, 4657–4667.
39 O. V. Prezhdo and P. J. Rossky, *J. Chem. Phys.*, 1997, **107**, 5863–5878.
40 J.-Y. Fang and S. Hammes-Schiffer, *J. Phys. Chem. A*, 1999, **103**, 9399–9407.
41 G. A. Fiete and E. J. Heller, *Phys. Rev. A*, 2003, **68**, 022112.
42 C. Zhu, S. Nangia, A. W. Jasper and D. G. Truhlar, *J. Chem. Phys.*, 2004, **121**, 7658–7670.
43 C. Zhu, A. W. Jasper and D. G. Truhlar, *J. Chem. Theory Comput.*, 2005, **1**, 527–540.
44 A. W. Jasper and D. G. Truhlar, *J. Chem. Phys.*, 2005, **123**, 064103.
45 G. Granucci and M. Persico, *J. Chem. Phys.*, 2007, **126**, 134114.
46 G. Granucci, M. Persico and A. Zoccante, *J. Chem. Phys.*, 2010, **133**, 134111.
47 J. E. Subotnik, W. Ouyang and B. R. Landry, *J. Chem. Phys.*, 2013, **139**, 214107.
48 A. Jain, E. Alguire and J. E. Subotnik, *J. Chem. Theory Comput.*, 2016, **12**, 5256–5268.
49 X. Gao and W. Thiel, *Phys. Rev. E*, 2017, **95**, 013308.
50 J.-K. Ha, I. S. Lee and S. K. Min, *J. Phys. Chem. Lett.*, 2018, **9**, 1097–1104.
51 B.-y. Xiao, J.-b. Xu and L.-j. Wang, *Chin. J. Chem. Phys.*, 2020, **33**, 603–612.
52 M. P. Esch and B. G. Levine, *J. Chem. Phys.*, 2020, **152**, 234105.
53 A. Sindhu and A. Jain, *J. Chem. Phys.*, 2023, **158**, 154109.
54 J. R. Mannouch and A. Kelly, *J. Phys. Chem. Lett.*, 2024, **15**, 11687–11695.
55 L. Dupuy, A. Rikus and N. T. Maitra, *J. Phys. Chem. Lett.*, 2024, **15**, 2643–2649.
56 E. Villaseco Arribas, N. T. Maitra and F. Agostini, *J. Chem. Phys.*, 2024, **160**, 054102.
57 E. Villaseco Arribas and N. T. Maitra, *Phys. Rev. Lett.*, 2024, **133**, 233201.
58 T. Tran, A. Ferté and M. Vacher, *J. Phys. Chem. Lett.*, 2024, **15**, 3646–3652.
59 G. Grell, J. González-Vázquez, F. Fernández-Villoria, A. Palacios and F. Martín, *J. Chem. Theory Comput.*, 2025, **21**, 10645–10668.
60 M. Cardosa-Gutierrez, R. D. Levine and F. Remacle, *J. Phys. B: At., Mol. Opt. Phys.*, 2024, **57**, 133501.
61 M. Cardosa-Gutierrez, G. Pandey, R. D. Levine and F. Remacle, *J. Phys. Chem. Lett.*, 2025, **16**, 7642–7648.
62 J. J. Bajo, G. Granucci and M. Persico, *J. Chem. Phys.*, 2014, **140**, 044113.
63 R. Mitrić, J. Petersen and V. Bonačić-Koutecký, *Phys. Rev. A*, 2009, **79**, 053416.
64 J. Petersen and R. Mitrić, *Phys. Chem. Chem. Phys.*, 2012, **14**, 8299–8306.
65 M. Richter, P. Marquetand, J. González-Vázquez, I. Sola and L. González, *J. Chem. Theory Comput.*, 2011, **7**, 1253–1258.
66 J. J. Bajo, J. González-Vázquez, I. R. Sola, J. Santamaria, M. Richter, P. Marquetand and L. González, *J. Phys. Chem. A*, 2012, **116**, 2800–2807.
67 B. Mignolet, B. F. E. Curchod and T. J. Martínez, *J. Chem. Phys.*, 2016, **145**, 191104.

View Article Online
DOI: 10.1039/D6FD00086J

68 B. Mignolet and B. F. E. Curchod, *J. Chem. Phys.*, 2018, **148**, 134110.

69 B. Mignolet and B. F. E. Curchod, *J. Phys. Chem. A*, 2019, **123**, 3582–3591.

70 J. Galiana, S. M. Cavaletto, G. Grell, F. Fernández-Villoria, A. Palacios, J. González-Vázquez and F. Martín, *J. Chem. Theory Comput.*, 2026, **22**, 1224–1243.

71 M. Ben-Nun and T. J. Martínez, *J. Chem. Phys.*, 1999, **110**, 4134–4140.

72 D. V. Shalashilin and M. S. Child, *J. Chem. Phys.*, 2008, **128**, 054102.

73 D. V. Makhov, W. J. Glover, T. J. Martinez and D. V. Shalashilin, *J. Chem. Phys.*, 2014, **141**, 054110.

74 C. D. Rankine, J. P. F. Nunes, M. S. Robinson, P. D. Lane and D. A. Wann, *Phys. Chem. Chem. Phys.*, 2016, **18**, 27170–27174.

75 L. M. Ibele, Y. Lassmann, T. J. Martínez and B. F. E. Curchod, *J. Chem. Phys.*, 2021, **154**, 104110.

76 Y. Lassmann, D. Hollas and B. F. E. Curchod, *J. Phys. Chem. Lett.*, 2022, **13**, 12011–12018.

77 P. A. Robertson, J. Merrick, D. Heathcote, M. S. Robinson, A. Butler, Y. Biddick, J. F. P. Nunes, C. Rankine, Z. Liu, S. F. Arrowsmith, J. O. F. Thompson, M. N. Murty, R. Chapman, E. Springate, E. A. Anderson, A. Kirrander and C. Vallance, *Chem. Phys. Lett.*, 2025, **871**, 142095.

78 J. González-Vázquez, *sharcdyn/sharc_public: Debug for MD-GAS 2023 Gdansk*, 2023, `https://doi.org/10.5281/zenodo.7352971`.

79 G. Granucci, M. Persico and A. Toniolo, *J. Chem. Phys.*, 2001, **114**, 10608–10615.

80 F. Plasser, G. Granucci, J. Pittner, M. Barbatti, M. Persico and H. Lischka, *J. Chem. Phys.*, 2012, **137**, 22A514.

81 B. O. Roos, P. R. Taylor and P. E. M. Siegbahn, *Chem. Phys.*, 1980, **48**, 157–173.

82 P.-Å. Malmqvist, A. Rendell and B. O. Roos, *J. Phys. Chem.*, 1990, **94**, 5477–5482.

83 G. Li Manni, I. Fdez. Galván, A. Alavi, F. Aleotti, F. Aquilante, J. Autschbach, D. Avagliano, A. Baiardi, J. J. Bao, S. Battaglia, L. Birnoschi, A. Blanco-González, S. I. Bokarev, R. Broer, R. Cacciari, P. B. Calio, R. K. Carlson, R. Carvalho Couto, L. Cerdán, L. F. Chibotaru, N. F. Chilton, J. R. Church, I. Conti, S. Coriani, J. Cuéllar-Zuquin, R. E. Daoud, N. Dattani, P. Decleva, C. de Graaf, M. G. Delcey, L. De Vico, W. Dobrautz, S. S. Dong, R. Feng, N. Ferré, M. Filatov(Gulak), L. Gagliardi, M. Garavelli, L. González, Y. Guan, M. Guo, M. R. Hennefarth, M. R. Hermes, C. E. Hoyer, M. Huix-Rotllant, V. K. Jaiswal, A. Kaiser, D. S. Kaliakin, M. Khamesian, D. S. King, V. Kochetov, M. Krośnicki, A. A. Kumaar, E. D. Larsson, S. Lehtola, M.-B. Lepetit, H. Lischka, P. López Ríos, M. Lundberg, D. Ma, S. Mai, P. Marquetand, I. C. D. Merritt, F. Montorsi, M. Mörchen, A. Nenov, V. H. A. Nguyen, Y. Nishimoto, M. S. Oakley, M. Olivucci, M. Oppel, D. Padula, R. Pandharkar, Q. M. Phung, F. Plasser, G. Raggi, E. Rebolini, M. Reiher, I. Rivalta, D. Roca-Sanjuán, T. Romig, A. A. Safari, A. Sánchez-Mansilla, A. M. Sand, I. Schapiro, T. R. Scott, J. Segarra-Martí, F. Segatta, D.-C. Sergentu, P. Sharma, R. Shepard, Y. Shu, J. K. Staab, T. P. Straatsma, L. K. Sørensen, B. N. C. Tenorio, D. G. Truhlar, L. Ungur, M. Vacher, V. Veryazov, T. A. Voß, O. Weser, D. Wu, X. Yang, D. Yarkony, C. Zhou, J. P. Zobel and R. Lindh, *J. Chem. Theory Comput.*, 2023, **19**, 6933–6991.

84 M. Barbatti and K. Sen, *Int. J. Quantum Chem.*, 2016, **116**, 762–771.

85 M. Ben-Nun and T. J. Martínez, *Chem. Phys. Lett.*, 1998, **298**, 57–65.

86 M. Ben-Nun, J. Quenneville and T. J. Martínez, *J. Phys. Chem. A*, 2000, **104**, 5161–5175.

87 G. A. Worth and I. Burghardt, *Chem. Phys. Lett.*, 2003, **368**, 502–508.

88 G. W. Richings, I. Polyak, K. E. Spinlove, G. A. Worth, I. Burghardt and B. Lasorne, *Int. Rev. Phys. Chem.*, 2015, **34**, 269–308.

89 S. M. Cavaletto, Z. Harman, T. Pfeifer and C. H. Keitel, *Phys. Rev. A*, 2017, **95**, 043413.

90 J. Janoš, P. Slavíček and B. F. E. Curchod, *J. Phys. Chem. Lett.*, 2024, **15**, 10614–10622.